NASA/TM-20230010737

Analytical Design and Performance Estimation Methods for Aircraft Permanent Magnet Synchronous Machines

Thomas F. Tallerico, Aaron D. Anderson, Matthew G. Granger, and Jonathan M. Gutknecht
Glenn Research Center, Cleveland, Ohio

September 2023

NASA STI Program . . . in Profile

Since its founding, NASA has been dedicated to the advancement of aeronautics and space science. The NASA Scientific and Technical Information (STI) Program plays a key part in helping NASA maintain this important role.

The NASA STI Program operates under the auspices of the Agency Chief Information Officer. It collects, organizes, provides for archiving, and disseminates NASA's STI. The NASA STI Program provides access to the NASA Technical Report Server—Registered (NTRS Reg) and NASA Technical Report Server—Public (NTRS) thus providing one of the largest collections of aeronautical and space science STI in the world. Results are published in both non-NASA channels and by NASA in the NASA STI Report Series, which includes the following report types:

- TECHNICAL PUBLICATION. Reports of completed research or a major significant phase of research that present the results of NASA programs and include extensive data or theoretical analysis. Includes compilations of significant scientific and technical data and information deemed to be of continuing reference value. NASA counter-part of peer-reviewed formal professional papers, but has less stringent limitations on manuscript length and extent of graphic presentations.

- TECHNICAL MEMORANDUM. Scientific and technical findings that are preliminary or of specialized interest, e.g., "quick-release" reports, working papers, and bibliographies that contain minimal annotation. Does not contain extensive analysis.

- CONTRACTOR REPORT. Scientific and technical findings by NASA-sponsored contractors and grantees.

- CONFERENCE PUBLICATION. Collected papers from scientific and technical conferences, symposia, seminars, or other meetings sponsored or co-sponsored by NASA.

- SPECIAL PUBLICATION. Scientific, technical, or historical information from NASA programs, projects, and missions, often concerned with subjects having substantial public interest.

- TECHNICAL TRANSLATION. English-language translations of foreign scientific and technical material pertinent to NASA's mission.

For more information about the NASA STI program, see the following:

- Access the NASA STI program home page at http://www.sti.nasa.gov

- E-mail your question to help@sti.nasa.gov

- Fax your question to the NASA STI Information Desk at 757-864-6500

- Telephone the NASA STI Information Desk at 757-864-9658

- Write to:
  NASA STI Program
  Mail Stop 148
  NASA Langley Research Center
  Hampton, VA 23681-2199

NASA/TM-20230010737

Analytical Design and Performance Estimation Methods for Aircraft Permanent Magnet Synchronous Machines

Thomas F. Tallerico, Aaron D. Anderson, Matthew G. Granger, and Jonathan M. Gutknecht
Glenn Research Center, Cleveland, Ohio

National Aeronautics and
Space Administration

Glenn Research Center
Cleveland, Ohio 44135

September 2023

This work was sponsored by the Advanced Air Vehicle Program
at the NASA Glenn Research Center

Level of Review: This material has been technically reviewed by technical management.

This report is available in electronic form at https://www.sti.nasa.gov/ and https://ntrs.nasa.gov/

Analytical Design and Performance Estimation Methods for Aircraft Permanent Magnet Synchronous Machines

Thomas F. Tallerico, Aaron D. Anderson, Matthew G. Granger, and Jonathan M. Gutknecht
National Aeronautics and Space Administration
Glenn Research Center
Cleveland, Ohio 44135

Abstract

The design of an electric motor drivetrain is a complex multiphysics problem. Low fidelity motor drivetrain sizing can be a key tool in the design cycle of an electric motor drivetrain and for system level studies of aircraft configurations. However, low fidelity sizing can lead to misleading results if all the physics involved in a motor design are not properly accounted for. This paper provides details on modeling approaches for initial design and sizing of permanent magnet synchronous electric machines. The goal of this paper is to provide the reader an understanding of the key principles of motor design and some modeling approaches to perform initial sizing of an electric motor and its inverter.

1.0 Introduction

The design of an electric motor drivetrain is a multiphysics problem that couples electromagnetics, heat transfer, fluid flow, structural mechanics, rotordynamics, materials, and power electronics. Neglecting any one of these disciplines in the design or sizing of an electric motor can lead to misleading or unrealistic performance predictions. Recently, increased interest in electric motors has been driven by their expected use in electric aircraft applications (Refs. 1 and 2). Electric aircraft sizing, control, system design, and system performance models all require some form of electric motor model or sizing methodology.

Commonly, vehicle sizing codes rely on motor sizing correlations based on torque scaling (Refs. 3 and 4) or constant power density (Ref. 5). These correlations neglect the effects of motor speed on mass and assign constant efficiencies not related to the mass of the motor. A number of analytical motor sizing examples for aircraft have been published (Refs. 6 to 10). These models frequently only focus on the electromagnetic performance of the machine and neglect motor thermal and/or structural performance and constraints. High fidelity motor drivetrain design codes similar to the ones developed at NASA's Glenn Research Center (Refs. 11 to 13) have significant computation cost that makes them impractical for aircraft system level studies or initial motor sizing.

In this paper, analytical sizing equations for permanent magnet synchronous machines and inverters are presented. Modeling details and trades are discussed to provide a reader who is not a motor designer some insight and understanding of the various models and equations. The models presented here are low fidelity models only intended for initial sizing and performance predictions. More complete discussions of motor design covering multiple machine topologies can be found in References 14 to 16. Mechanical gears are often used to reduce required motor torque and overall motor drivetrain weight but are not covered in this paper. Reference 17 gives a commonly used correlation for gear weight, (Ref. 18) gives a genetic optimization design procedure for mechanical gearboxes, and Reference 19 gives a detailed discussion of gearing theory.

This paper is organized such that Section 2.0 shows a reference motor geometry, Section 3.0 discusses motor electromagnetic analytical sizing, Section 4.0 discusses motor thermal considerations, Section 5.0 discusses motor mechanical considerations, Section 6.0 discusses inverter design, and Section 7.0 has a brief conclusion.

2.0 Motor Geometry

The motor topology discussed in this paper is a permanent magnet synchronous machine (PMSM). Figure 1 shows the basic geometry of a concentrated wound, in-runner motor of this type. The depicted example machine uses a Halbach array for its magnetic rotor and retains the magnets with a carbon fiber retaining hoop. A finned water jacket heat sink is used to cool the machine. The basic dimensions of the machine are labeled to provide clarity for how the machine dimensions are defined in this paper.

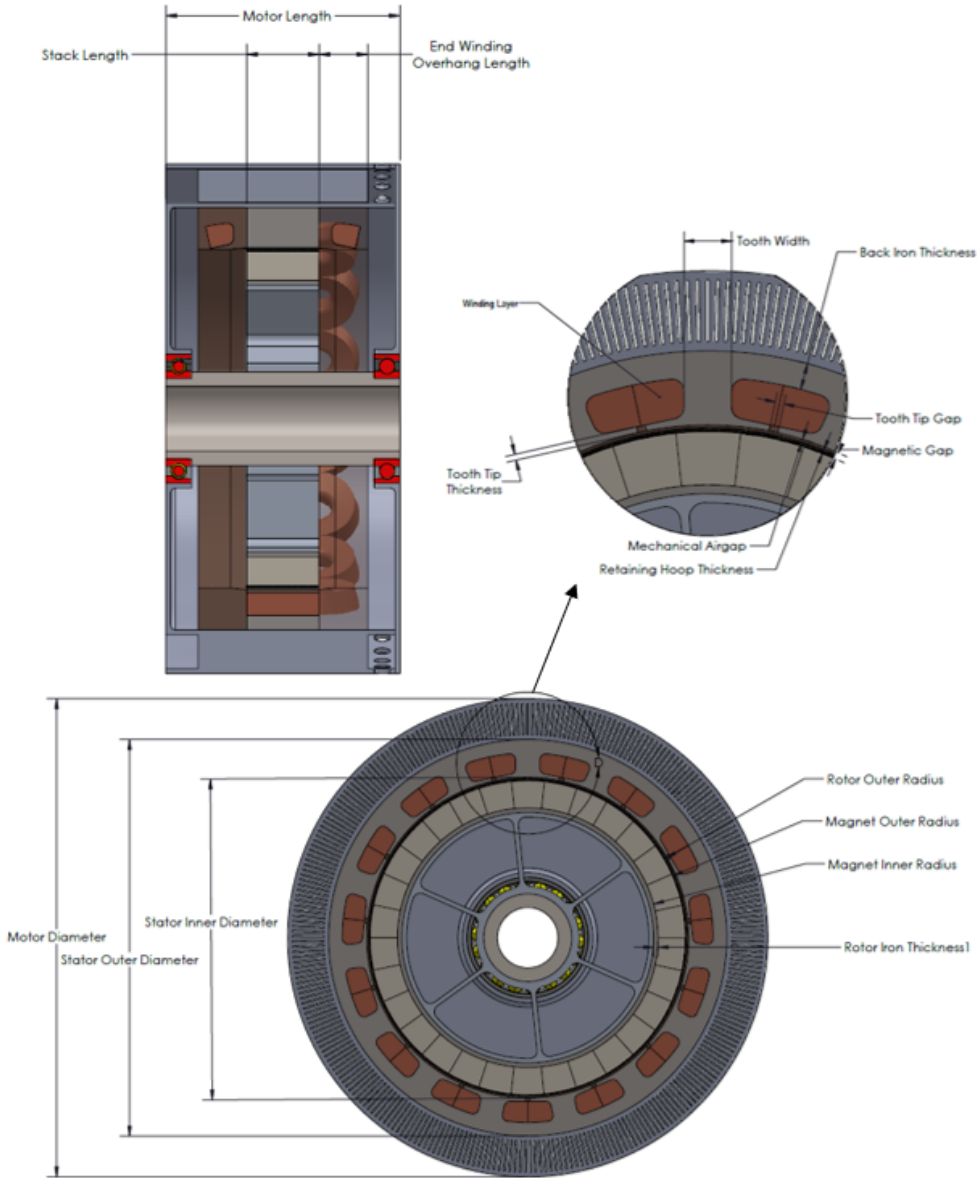

Figure 1.—Example Geometry for a Halbach array permanent magnet inner rotor machine. Definitions of various geometric parameters defining a machine are provided.

3.0 Electromagnetic Motor Sizing

3.1 The Basic Motor Sizing Equation

A common equation used in the sizing of an electric motor is the D^2L sizing equation (Ref. 14):

$$P = \omega\tau = \omega\frac{\pi}{2}(\bar{B}\bar{A})D^2L \tag{1}$$

where P is motor power, ω is rotor angular velocity, τ is torque, $\bar{B}$ is the average magnitude of the radial flux density produced by the rotor, $\bar{A}$ is the stator electrical loading, D is the stator inner diameter, and L is the motor stack length (Ref. 14).

The above equation can be understood in the following manner:

- ω is the speed term that determines the power produced by a given torque. The remaining terms in the equation define the torque produced by the motor.
- $\frac{D}{2}$ can be factored out as the radius of the rotor which is the lever arm the motor uses to produce torque.
- The remaining terms, $\pi(\bar{B}\bar{A})DL$, is the force generated between the rotor and the stator and is equivalent to $B \times IL$, the force generator on a wire of length L perpendicular to a field B and carrying current I. How B and L translate in between the two forms of this force expression is apparent. The remaining terms, $\pi\bar{A}D$, are equivalent to I, the current, in the $B \times IL$ formulation.
- $\bar{A}$ the electrical loading is the current per unit circumference that interacts with the B field to create force. $\bar{A}$ is given by

$$\bar{A} = \frac{k_w I_{tot}}{\pi D} \tag{2}$$

  Where I_{tot} is the total current that passes through the stator in both axial directions and k_w is the winding factor.
- The winding factor defines the percent of the flux produced by a given stator winding that interacts with the rotor flux to produce torque. Put another way, it defines how well a given winding layout produces flux with the same matching spatial harmonic order as the pole count of the rotor. k_w typically has values in the range of 0.85 to 1. It can be calculated manually or is readily available in various publications for most motor slot pole combinations. Table 1 gives some typical values for k_w from Reference 20.

TABLE 1.—COMMON SLOT POLE COMBINATIONS AND WINDING FACTOR VALUES

Slots per pole per phase	k_w	Slots per pole per phase	k_w
1/2 and 1/4	0.866	3/8 and 3/10	0.945
3/7 and 3/11	0.902	5/14 and 5/16	0.951
2/5 and 2/7	0.933	Distributed full pitch windings	0.95 to 1.00

Lipo (Ref. 15) provides a slightly different formulation of Equation (1)

$$P = \omega \frac{\pi}{4} (B_{g1} K_{s1}) D^2 L \tag{3}$$

Where B_{g1} is the peak magnetic flux density of the fundamental harmonic produced by the rotor and K_{s1} is the peak fundamental value of the linear current density. For a permanent magnet machine with full magnet surface fill on the rotor B_{g1} relates to $\bar{B}$ (a uniform magnitude magnetic field)

$$B_{g1} = \frac{4\bar{B}}{\pi} \tag{4}$$

K_{s1} relates to $\bar{A}$ by accounting for the difference between peak and average current of a sinusoidal waveform

$$K_{s1} = \bar{A} \frac{\pi}{2} \tag{5}$$

3.1.1 Power and Torque Density

Equation (1) is frequently used to roughly size a machine to maximize torque per unit volume (torque density) or power per unit rotor volume (power density) and can be rewritten as

$$PowerDensity = \omega * TorqueDensity = \omega \frac{1}{2} (\bar{B}\bar{A}) D \tag{6}$$

Both power density and torque density, while relevant metrics, are not as important to aircraft applications as specific power or specific torque (power and torque per unit mass). Optimizing for volume and optimizing for mass are typically competing objectives in the design of an electric machine. Maximizing power density or torque density will favor maximizing the amount of magnetic material in a volume which is typically not mass optimum for a motor. This trade is especially true for permanent magnet machines since magnets get less mass efficient at producing flux as they get thicker (see Section 3.2.1.1).

From Equation (1), $\bar{B}\bar{A}$ is often referred to as the magnetic shear stress of a motor and is frequently used as a rating metric for machines. Maximizing it will maximize the power/torque density of a machine at a given diameter and speed. As a result, aircraft machines which target high specific power, will have lower magnetic shear stresses than terrestrial machines designed to maximize power/torque density if designed with the same technologies. In general, for aviation machines it is best to calculate metrics per unit mass directly. Calculating machine mass requires explicit design or explicit assumptions about the geometry of the machine.

3.1.2 Efficiency and Power Factor

Equation (1) is commonly written with efficiency and/or power factor in the formulation. Whether to include efficiency is a matter of how the equations are implemented. Equation (1) defines torque and power in the absence of magnetic losses and mechanical losses. Magnetic losses (eddy currents and stator iron losses) reduce the flux density produced by the rotor and stator in the airgap and result in reduced torque production. Mechanical losses (windage and bearing losses) act as drag on the rotor and reduce the available output torque of the motor at the shaft. Both of these power losses result in a need to increase stator electrical loading to meet the output power target of the machine. This can be accounted for by rewriting Equation (1) as

$$P_{out} + Loss_{speed} = \omega \left(\tau_{out} + \frac{Loss_{speed}}{\omega} \right) = \omega \frac{\pi}{2} (\bar{B}\bar{A}) D^2 L \tag{7}$$

where $Loss_{speed}$ are the sum of the magnetic and mechanical power losses at the rotational speed ω. They are labeled $Loss_{speed}$ because they are predominantly a function of the rotational speed of the rotor in permanent magnet machines; however, magnetic losses will have some dependance on the electrical loading of the machine as stator current increases the amount of time varying flux in the machine's magnetic components.

Power factor defines the ratio between real power and apparent power and is defined as

$$PF = \frac{P}{S} \tag{8}$$

where P represents real power and S represents apparent power. Real power is what the machine outputs and is the time average of the instantaneous electrical input power, given by

$$P = \frac{1}{T}\int_0^T i\ v\ dt \tag{9}$$

where i and v are time-varying current and voltage functions, t is time, and T is the total time average power is being calculated over. Apparent power is the product of the amplitudes of applied current (I) and voltage (V) given by

$$S = IV \tag{10}$$

Reactive power, Q, is power that goes into stored energy in the machine as each coil is excited and then is returned to the supply as the coil is de-energized. Real, apparent, and reactive power are related by

$$S^2 = P^2 + Q^2 \tag{11}$$

Equation (1) only accounts for real power. The required power supply to drive a given machine is sized based on apparent power, so power factor should be accounted for when doing system level sizing of motor drivetrains to accurately size the components on the aircraft. Power factor will directly affect the inverter switching losses and required size of DC link capacitors in the inverter (Section 6.0). Power factor can be calculated using per phase circuit analysis of the real and reactive power. For initial sizing of a motor however it can be sufficient to estimate the power factor using common values for different machine types. Power factors for permanent magnet synchronous machines are typically greater than 0.90.

3.2 Calculation of the Average Magnitude of the Radial Flux Density Produced by the Rotor, $\bar{B}$

The average value of the radial flux density produced by the rotor, $\bar{B}$ in Equation (1), can be calculated in low fidelity sizing of permanent magnet machines using either magnetic reluctance networks or closed form analytical solutions to Maxwell's equations. The following sections discuss magnet reluctance networks and provide an example closed form solution. Higher fidelity finite element analysis (FEA) calculations can also be used to calculate B with higher accuracy, example models and methods of sizing machines with FEA based calculations are given in References 11 to 13.

3.2.1 Magnetic Reluctance Networks

Magnetic reluctance networks or equivalent magnetic circuits discretize a motor into magnetic resistances and source (magnetomotive force) terms so that the flow of flux in the motor can be solved for

in the same way current is solved for in an electric circuit. The basic equation of magnetic reluctance networks is

$$\varphi = \frac{MMF}{R} \tag{12}$$

where φ is the magnetic flux through the reluctance path, *MMF* is magnetomotive force applied to the reluctance path, and *R* is the magnetic reluctance of the path (Ref. 14). φ, the magnetic flux, relates to *B*, the magnetic flux density, by

$$B = \frac{\varphi}{A} \tag{13}$$

where *A* is the cross-sectional area of the reluctance path.

MMF for a coil is defined as

$$MMF = NI \tag{14}$$

where N is the number of turns and *I* is the current in each turn.

MMF for a magnet is defined as

$$MMF = \frac{Br}{\mu_0 \mu_r} l_m \tag{15}$$

where Br is remnant flux density, μ_0 is the permeability of free space, μ_r is the relative permeability of the magnetic material, and l_m is the thickness of the magnet or the size of the element if multiple elements span a magnet. *R*, the reluctance of a given path or given reluctant element is given as

$$R = \frac{l}{A \mu_0 \mu_r} \tag{16}$$

where l is the length of the path and *A* is the cross-sectional area of the path perpendicular to length l.

Reluctance networks can be made as simple or as complex as necessary depending on whether the objective of the sizing is fast computational time or high accuracy. The iron in a machine can often be treated as infinitely permeable in these models since it has a relative permeability orders of magnitude greater than that of air and permanent magnet materials. Notable examples where iron cannot be modeled as infinitely permeable would be in machines that are saturated, stator tooth tips that are often saturated, and the design of buried permanent magnet machines where saturating the rotor iron is necessary to get field across the airgap of the machine (Ref. 7).

3.2.1.1 Simple Example of North South Array

The simplest magnetic network that can be used to represent a permanent magnet machine and define the flux in the magnetic airgap of the machine is depicted in Figure 2. The model is for a traditional north south rotor magnetic array. A single flux path is assumed. All leakage flux paths are neglected and only the field produced by the rotor magnets is accounted for.

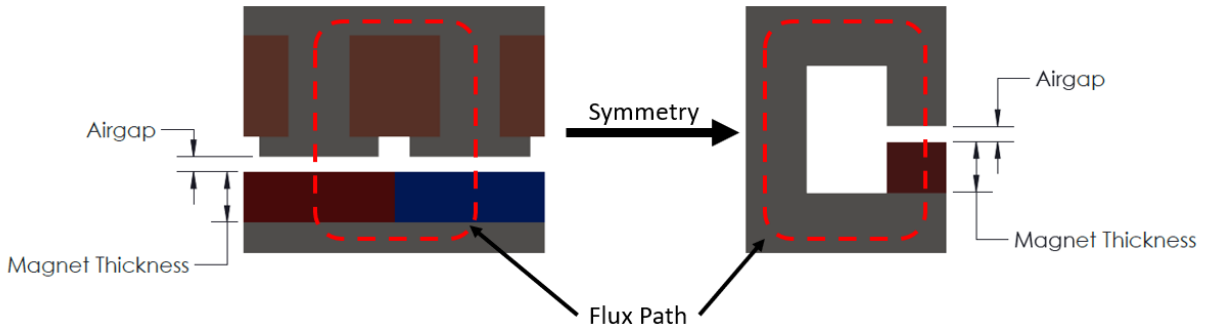

Figure 2.—Simple Magnetic Reluctance Network for a N-S Magnet Array. Left shows full geometry. Right shows the simplified model that can result from the use of symmetry.

The reluctance of the path is assumed to be the sum of the magnet and airgap reluctance. The reluctance of the iron is neglected. For the full model (without symmetry) the reluctance can be written as

$$R = 2 * R_{ag} + 2 * R_{mag} = \frac{2l_g}{A_m \mu_0} + \frac{2l_m}{A_m \mu_0 \mu_r} \tag{17}$$

where l_g is the airgap size and A_m is the magnet area.

The magnetomotive force in the circuit is equal to

$$MMF = 2\frac{Br}{\mu_0 \mu_r} l_m \tag{18}$$

The flux in the path is then given by

$$\varphi = \frac{MMF}{R} = \frac{2\frac{Br}{\mu_0 \mu_r} l_m}{\frac{2l_g}{A_m \mu_0} + \frac{2l_m}{A_m \mu_0 \mu_r}} = \frac{\frac{Br}{\mu_r} l_m A_m}{l_g + \frac{l_m}{\mu_r}} \tag{19}$$

The last form of the above equation is equivalent to the simpler magnetic circuit depicted in Figure 2 as symmetry enables simplification of the model. The field in the gap produced by the magnets can then be defined as

$$B_m = \frac{Br l_m}{l_g \mu_r + l_m} \tag{20}$$

Where B_m is the airgap field produced by the magnets. For rotors where magnets span the full magnetic pole B_m will be equal to $\bar{B}$. For rotors where the magnets do not span the full magnetic pole, Lipo (Ref. 15), provides an expression for B_{g1},

$$B_{g1} = \frac{4}{\pi} B_m \sin\left(\frac{\alpha_m}{2}\right) \tag{21}$$

where B_{g1} is the peak flux density magnitude of the fundamental harmonic, α_m is the magnet's pole span angle in electrical degrees. Equations (20) and (21) are reasonably accurate for an initial motor sizing as long as the iron in the machine is operated below saturation and the airgap is at least an order of magnitude smaller than the pole-to-pole distance in the machine. Because leakage is neglected,

Equations (20) and (21) will always overpredict *B* and result in some underprediction of the required current in the stator.

Equation (20) can provide some good insight into the effect or magnet thickness on the performance of a motor. Figure 3 shows *B* versus magnet thickness for a 1 mm air gap, a magnet with a remnant flux density of 1.2 T, and a magnet relative permeability of 1.05. In Figure 3, increasing magnet thickness results in increased gap flux density, but the marginal gains that result from increasing magnet thickness decrease rapidly at larger magnet thicknesses. Magnetic field density per magnet thickness is also plotted in Figure 3. Field density per magnet thickness is shown to always decay with increasing magnet thickness. This decay is the result of magnet material having a permeability similar to that of air. Correspondingly, increasing magnet thickness increases the reluctance of the flux path and reduces the effectiveness of the magnet material.

Field density per magnet thickness is analogous to the specific flux (flux per mass) of a magnet. Specific flux per magnet thickness always decays as magnet thickness increases. The most mass efficient magnet in terms of specific flux is infinitely thin. In the design of a machine, the weight of the other components in the machine and efficiency goals will cause some magnet thickness greater than zero to be optimum. The trend of magnets becoming less mass effective as they increase in thickness is important to understand and as mentioned previously is a key difference between volume and mass optimization of motors.

More complex reluctance networks can be created to capture field leakage or obtain more information about the field in the magnetic components of the motor (Refs. 10 and 7). For buried permanent magnet rotors, saturation effects and non-linear solvers are needed to capture the field leakage through the bridges of the rotor iron. At some point, as the fidelity of a reluctance network increases, the relative computational cost associated with a finite element solution becomes insignificant, and the benefit of a low fidelity model is diminished.

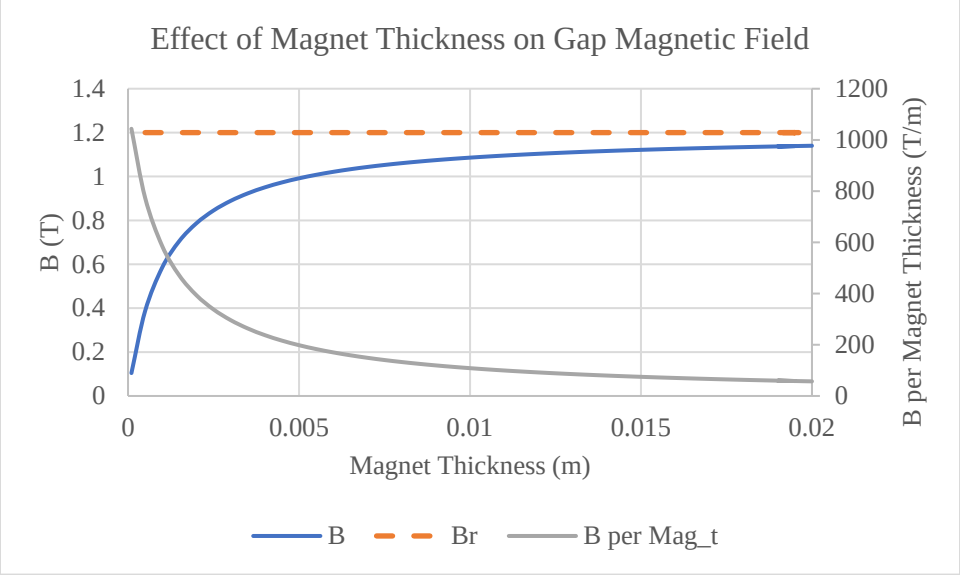

Figure 3.—Effect of magnet thickness on airgap flux density based on the simple reluctance model of Figure 2.

3.2.1.2 Stator Inductance Calculation

The inductance of a stator coil can also be estimated using reluctant networks. For the geometry in Figure 4 paths across the tooth tips and to-and-from the rotor back iron can be accounted for and summed as resistors in parallel, so that the reluctance one coil sees is given by

$$R = \frac{1}{\frac{2}{R_{tip}} + \frac{1}{R_{rotor}}} = \frac{1}{\frac{2A_{tip}\mu_0}{l_{tip}} + \frac{3}{2}\frac{W_{sp}Stack\mu_0}{l_m + l_g}} \tag{22}$$

where A_{tip} is the tooth tip area (tooth tip thickness times stack length), l_{tip} is the tooth tip gap width, and W_{sp} is the stator pole width. The self-inductance of a single coil can then be calculated as

$$L_m = \frac{N * \varphi}{I} = \frac{I * N^2}{I * R} = N^2 * \left(\frac{2A_{tip}\mu_0}{l_{tip}} + \frac{3}{2}\frac{W_{sp}Stack\mu_0}{l_m + l_g}\right) \tag{23}$$

where N is the number of turns in the active coil.

Equation (23) is the self-inductance of a single stator coil. Mutual inductance to each of the adjacent coils can be approximated as half of self-inductance for the geometry in Figure 4 assuming all the coils have the same number of turns. The inductance of the motor is a key variable for motor drive sizing as discussed in Section 6.0. The field produced by the stator coils can also be included in the sizing of a motor's iron components and the corresponding iron loss predictions (Section 3.3). Equation (23) only accounts for the magnetizing inductance of the motor. Additional leakage inductance will exist in a motor, especially in the end windings of the machine. Leakage inductance can be neglected, accounted for based on correlations for different machine types, or calculated using more complex 3D reluctance or FEA models of the motor.

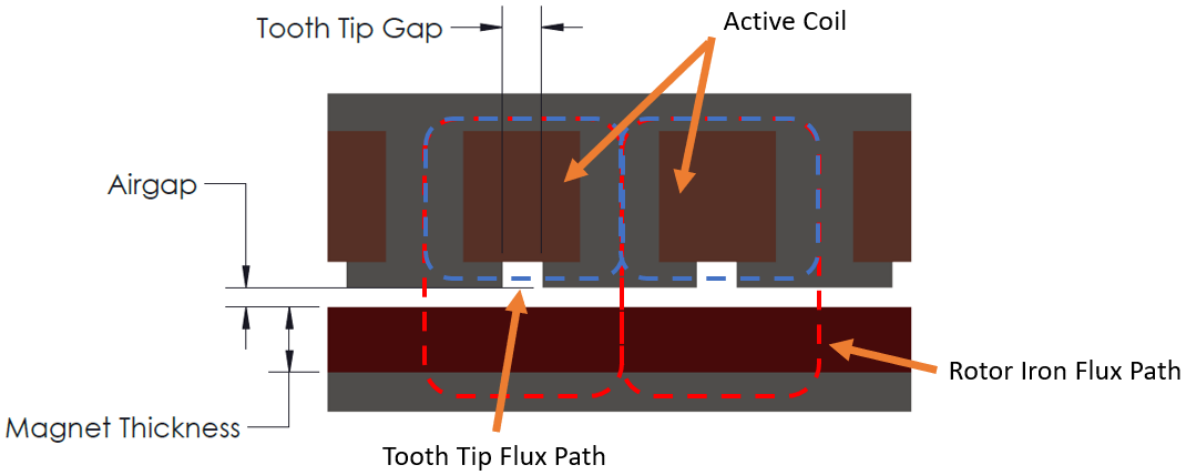

Figure 4.—Flux Paths for Low Fidelity Stator Inductance Calculation.

3.2.2 Closed Form Field Solutions

Closed form solutions for the field produced by permanent magnet rotors can be found in the literature or derived using Maxwell's equations. One example case for Halbach arrays is given in Reference 21. Multiple solutions for different machine types are summarized. The solution for the radial airgap field from iron cored Halbach machines is

$$B_r(r,\theta) = \frac{Br\left(\frac{p}{p+1}\right)\left(1-\left(\frac{R_r}{R_m}\right)^{p+1}\right)}{1-\frac{R_r}{R_s}^{2p}}\left(\left(\frac{r}{R_s}\right)^{p-1}\left(\frac{R_m}{R_s}\right)^{p+1}+\left(\frac{R_m}{r}\right)^{p+1}\right)\cos(p\theta) \tag{24}$$

where p is pole count, R_m is the magnet outer radius, R_r is the magnet inner radius, and R_s is the stator inner radius. The average airgap field from this equation can be calculated as

$$\bar{B} = \frac{2}{\pi}Br(R_s,0) \tag{25}$$

Equation (24) assumes infinite iron permeability and a magnet permeability equal to 1. It does account for airgap field leakage and is correspondingly more accurate than the simple reluctance network presented in the prior section. Equation (24) can also be used to compute the field that interacts with the windings in an air-core stator. In that case Equation (1) is not as easily applied and it is more appropriate to integrate $B \times IL$ in the winding domain to calculate tangential magnetic forces.

3.2.3 Magnet Remnant Flux Density *Br*

Magnet remanent flux density is a material property of permanent magnets. It depends on the magnet grade and the temperature the magnet operates at. Magnet grade/material must be selected such that sufficient temperature margin is maintained in a worst-case operating condition for the machine. Once a magnet material is selected, *Br* at operating temperature will be given by

$$Br_T = Br_{20C} - \alpha_{mag}(T-20C)Br_{20C} \tag{26}$$

where Br_T is the magnet remnant flux density at temperature, Br_{20C} is the remnant flux density at 20 °C, T is temperature in Celsius, and α_{mag} is a material property related to the specific magnet grade (Ref. 22).

If designing for continuous operation with cooling of the rotor through the stator only, the magnets may be at a temperature greater than the stator and the magnets must be designed for that condition. If designing for transient mission profiles, the magnet temperature will lag the temperature of the stator and can be designed for a lower temperature. In general, SmCo magnets are a good option to avoid demagnetization of the magnets in operation while NdFeB magnets offer higher performance at moderate operating temperatures. With temperature and magnet fill knockdowns for laminations and tolerances, *Br* will generally be in the 1 to 1.1 Tesla range.

3.2.4 Airgap Size

Typically, the mechanical airgap in a motor is around 1 mm. The magnetic gap in the machine is the sum of the mechanical airgap and the needed non-magnetic mechanical components to retain the magnets centripetal loading (Section 5.1). Smaller than 1 mm airgaps can be beneficial when the pole-to-pole distance is on the same order of magnitude as the gap size. Smaller gap sizes can enable a reduction in

magnet thickness needed to reach a desired $\bar{B}$, but since the magnet thickness is a part of the magnetic airgap, the reduction in needed thickness is only significant for a thin magnetic array. Mechanical tolerance stack ups, mechanical deflections, and thermal expansion/contraction limit how small of an airgap can practically be used in a machine. Additionally, windage loss (Section 5.2) may result in a larger airgap being optimal for very high speed machines.

3.3 Magnetic Losses

With the field from the rotor known, magnetic losses in the stator iron can be calculated. Iron losses are typically the largest loss other than stator resistive losses in a motor. Other magnetic losses like rotor magnet loss, rotor iron loss, and winding proximity loss are difficult to calculate unless a time stepping magnet model is used to compute the time varying fields in the components. Neglecting them in an initial sizing for an aircraft motor is not a major source of error since rotor losses can be suppressed to very low values using fine laminations and winding proximity losses can be suppressed by using fine gage or litz wire in the stator windings. Rotor iron loss is generally small in a synchronous permanent magnet machine since most of the flux the rotor iron sees comes from the rotor magnets which rotates with it.

Stator iron losses relate to the motion of electrons in the iron as it magnetizes. Iron loss is typically estimated using the Steinmetz equation

$$P_v = k f^{\alpha} B^{\beta} \tag{27}$$

where P_v is the iron loss per volume, f is the frequency of the magnetic field, B is the peak magnetic flux density, and k, α, and β are the Steinmetz coefficients (Ref. 23). The coefficients k, α, and β are found by completing a curve fit to iron loss data found in electrical steel data sheets. The loss data in these data sheets is collected by testing magnetic cores of the material using unidirectional fields. ASTM A697 (Ref. 24) is the typical standard governing the testing. Because of the idealized scenario with which magnetic material loss data is collected, it is not uncommon for iron losses to be greater than predicted using the Steinmetz equation (Ref. 23).

Other equations with more terms can be used to fit to manufacturer provided data. A common alternative form is the Bertotti expression

$$P_v = k_h f B^{\beta} + k_c f^2 B^2 + k_e f^{1.5} B^{1.5} \tag{28}$$

where loss terms are broken out to hysteresis, eddy, and excess loss components each with their own coefficients (Ref. 25). The added terms can make it easier to curve fit to the iron loss data over a larger range. At higher frequencies the eddy current loss term in this formulation can be corrected to account for skin depth (Ref. 26). Either form of curve fit can work for iron losses as long as it accurately matches the available experimental data in the range relevant to the field magnitude and electrical frequency of the machine. Many other iron loss models exist. A comparison of some of the most common models can be found in Reference 27.

The iron losses of a stator are broken into back iron and tooth iron losses since the rate of magnetization and the magnitude of peak magnetic field is different in each component. For the back iron, the peak field in the back iron can be calculated as

$$B_{back} = \frac{\varphi_{back}}{A_{back}} = \frac{\bar{B}}{L * t_{back}} * \frac{2\pi R_s}{2p} * L = \frac{\bar{B}}{t_{back}} * \frac{2\pi R_s}{2p} \tag{29}$$

where B_{back} is the peak field in the stator back iron, φ_{back} is the peak flux in the stator back iron, A_{back} is the back iron cross sectional area, L is stack length, and R_s is stator inner radius. Here $\frac{2\pi R_s}{p} L\bar{B}$ represents the flux per pole that is produced in the airgap by the rotor. The frequency of magnetization in back iron is equivalent to the fundamental frequency in the machine.

The peak field in the tooth iron can be estimated as

$$B_{tooth} = \frac{\varphi_{tooth}}{A_{tooth}} = \begin{cases} \frac{\bar{B}}{w_{tooth}} * \frac{2\pi R_s}{p}, & Slots < (2 * p) \\ \frac{\bar{B}}{w_{tooth}} * \frac{2\pi R_s}{p} * \left(\frac{p}{Slots - p}\right), & Slots \geq (2 * p) \end{cases} \tag{30}$$

where B_{tooth} is the peak field in the stator tooth iron, φ_{tooth} is the peak flux in the stator tooth iron, and A_{tooth} is the tooth iron cross sectional area Stator teeth magnetize at a faster rate than the back iron and then stay at peak magnetic field or zero magnetic field for some amount of time. The flux density in the tooth can be assumed to have a trapezoidal shape with time. The effective frequency of magnetization of the tooth is equivalent to the tooth passage frequency relative to the rotor. It can be calculated as

$$f_{tooth} = f_{nom} * \frac{Slots}{2 * p} \tag{31}$$

This frequency accounts for the increased rate of magnetization, but since the frequency of the machine is still f_{nom} a correction must be applied to the iron loss equations such that the loss in the stator teeth per unit volume is given as

$$P_{v_{thooth}} = \frac{f_{nom}}{f_{tooth}} k f_{tooth}^{\alpha} B^{\beta} \tag{32}$$

in the Steinmetz formulation of the loss equation.

3.4 Calculating Current and Resistive Losses

Once $\bar{B}$ from the rotor is calculated, the dimensions of a machine and the speed losses can be used to solve for $\bar{A}$ using Equation (7) for a desired output torque. Equation (2) can then be used to solve for the total current in the machine I_{tot}. The average current per slot per winding layer can then be calculated as

$$I_{avg,layer} = \frac{I_{tot}}{Slots * Layers} \tag{33}$$

where $I_{avg,layer}$ is the average current per winding layer, *Slots* is the number of winding slots, and $Layers$ is the number of winding layers per slot. Typically, layers will be 2 for concentrated wound machines or 1 for distributed wound machines.

For a 3-phase motor with sinusoidal supply currents the peak current per winding layer can be calculated as

$$I_{peak,layer} = \frac{\pi}{2} I_{avg,layer} \tag{34}$$

where $I_{peak,layer}$ is the peak current per winding layer. The root mean squared current per layer can be calculated as

$$I_{rms,layer} = \frac{1}{\sqrt{2}} I_{peak,layer} \tag{35}$$

The resistive losses in the motor can then be estimated as

$$Loss_{I2R} = Slots * Layers * \rho_{copper} * \frac{L_{Layer}}{SF * A_{Layer}} I_{rms,layer}^2 \tag{36}$$

where ρ_{copper} is the resistivity of copper, L_{Layer} is the length of a layer, A_{Layer} is the layer cross-sectional area, and SF is the copper slot fill. L_{Layer} is equal to the stack length of the machine plus the average length of one end turn of the machine. *SF*, the copper slot fill, will typically fall in the range of 35 to 55 percent for motors wound with round conductors. Higher fill factors can be achieved with hairpin or bar windings, but AC losses need to be accounted for when designing windings of that type. As a conservative first estimate 40 percent can be used for winding fill in initial sizing.

Copper resistivity variation with temperature should be accounted for when calculating loss. The resistivity of copper at a given temperature can be calculated based on its resistivity at 20 °C and the assumed temperature of the winding.

$$\rho_{copper,T} = \rho_{copper,20C} * \left(1 + 0.00393(T - 20°\mathrm{C})\right) \tag{37}$$

If a motor is being designed for multiple mission design points magnetic, mechanical, and resistive losses can be calculated for each mission point by repeating the calculations for each operating condition. Similarly, efficiency maps can be built by repeating the calculation for all relevant operating conditions.

3.4.1 AC Winding Loss

AC winding losses can be a major loss component in a machine and can drive the design of the winding in terms of wire size, number of wire strands wound in parallel, and twist/transposition of the wire strands. Typically, good winding design can minimize AC losses to less than 1 percent of total machine losses. Correspondingly, it is typical to neglect AC winding losses in initial machine sizing, especially since design of individual conductors is required to estimate loss. A few equations for AC winding losses are provided here for completeness.

AC winding losses can be separated into two orthogonal components: skin effect and proximity effect (Ref. 28). For round conductors, the AC resistance due to skin effect can be related to the DC resistance of the winding by

$$R_{ac} = \frac{R_{dc}}{2} * \frac{\gamma\left(ber(\gamma)bei'(\gamma) - bei(\gamma)ber'(\gamma)\right)}{ber'^2(\gamma) + bei'^2(\gamma)} \tag{38}$$

where *bei* and *ber* equations are Kelvin functions (Ref. 29) and γ is defined as

$$\gamma = \frac{d}{\delta\sqrt{2}} \tag{39}$$

where d is the diameter of the conductor and δ is the skin depth in the material at the frequency current is being applied to the conductor (Ref. 28). The proximity loss per unit stack length in a conductor can be written as

$$P_{prox} = \frac{2\pi\gamma}{\sigma} \frac{\left(ber_2(\gamma)ber'(\gamma) + bei_2(\gamma)ber'(\gamma)\right)}{ber^2(\gamma) + bei^2(\gamma)} H_e^2 \tag{40}$$

where σ is the material conductivity and H_e is the peak value of the applied external magnetic field (Ref. 28). When the source of external field on the conductors in a winding is the field from the other

conductors in the same slot of the machine Equation (38) and (40) can be integrated into a single expression for the AC resistivity of the m^{th} layer of conductors in the slot

$$R_{ac} = \frac{R_{dc}}{2}\gamma\left(\frac{\left(ber(\gamma)bei'(\gamma) - bei(\gamma)ber'(\gamma)\right)}{ber'^2(\gamma) + bei'^2(\gamma)} - 2\pi(2m-1)^2\frac{\left(ber_2(\gamma)ber'(\gamma) + bei_2(\gamma)ber'(\gamma)\right)}{ber^2(\gamma) + bei^2(\gamma)}\right) \quad (41)$$

where m is the layer number (Ref. (28).

Often, to suppress AC losses, wire gage is selected such that $d < \delta$. However, when small strand size is used, a number of wires have to be wound in parallel and circulating currents between phases due to uneven magnetic potential can cause additional AC losses. The most common solution to this problem is to twist the small strands that are in parallel together so that their magnetic potential is balanced over the length of the wire. This type of wire construction is often referred to as litz wire. Reference (30) gives a design guide for litz wire windings. The AC resistance of the winding with $d < \delta$ is expressed as

$$R_{ac} = R_{dc}\left(1 + \frac{(\pi n N_s)^2 d^6}{192 * \delta^4 b^2}\right) \quad (42)$$

where n is the number of strands, N_s is the number of turns, and b is the winding width.

One particular case where twist cannot be used to balance the magnetic potential between parallel paths in the same winding is hairpin windings. In this case careful conductor placement has to be used to balance the potential between windings. Reference (31) provides a design guide for hairpin windings.

For external sources that produce a time varying field on round conductors, the proximity loss per unit length generated in a round conductor can be written as

$$P_{prox} = \frac{\pi^2 \sigma d^4}{32}(fB)^2 \quad (43)$$

when $d < \delta$(Ref. (32).

3.5 Voltage and Turn Count

Outside of the discussion of power factor, voltage has not been mentioned in any of the above equations, because its impact on machine mass and efficiency is only through secondary effects on slot fill and ac winding loss. Machine voltage does have significant effects on the sizing of the inverter (Section 6.0) and the DC bus of a vehicle. In most cases, motor winding turn count can be increased or decreased to match the voltage requirements of a given vehicle and motor drive without significantly effecting the mass and efficiency of the motor. The voltage of a machine can be expressed in the *d-q* frame of the machine as

$$V_{ph} = \sqrt{V_q^2 + V_d^2} \quad (44)$$

where V_{ph} is the peak per phase motor voltage, V_q is the q axis voltage of the machine, and V_d is the d axis voltage of the machine (Ref. 16). The *d-q* reference frame of a machine is a reference frame of a motor where the 3-phase circuit components of a machine appear to be invariant with time. For synchronous machines, the *d-q* reference frame aligns with the rotating frame of the rotor. The *d* or direct axis aligns with rotor poles and the *q* or quadrant axis is orthogonal to the *d* axis. A Park transformation can be used to translate the per phase circuit variables to the *d-q* frame (Ref. 33).

V_q and V_d can be written as

$$V_q = EMF_i + X_d I_d + R_s I_q \quad (45)$$

$$V_d = X_q I_q + R_s I_d \quad (46)$$

where EMF_i is the per phase back electromotive force of the motor, X_d is the d axis reactance of the motor, X_q is the q axis reactance, R_s is the stator resistance, I_q is the q axis current, and I_d is the d axis current. For surface permanent magnet synchronous machines without rotor saliency, max torque per ampere is achieved when I_d is zero. Correspondingly, V_q, V_d, and V can be reduced to

$$V_q = EMF_i + R_s I_s \tag{47}$$

$$V_d = X_q I_s \tag{48}$$

$$V_{ph} = \sqrt{(EMF_i + R_s I_s)^2 + \left(X_q I_s\right)^2} \tag{49}$$

where I_s is the motor supply current.

3.5.1 Back EMF

The back EMF of the motor can be derived by putting Equation (1) into terms of supply current and voltage

$$P = \frac{3}{2} EMF_i I_s = \frac{2}{\pi} \omega D L k_w \bar{B} N_t N_p I_s = \frac{\omega D L k_w B_{g1}}{2} N_t N_p I_s \tag{50}$$

where EMF_i is the per phase back emf, I_s is the motor supply current, N_t is the number of series connected turns per phase, and N_p is number of phases (Ref. 16). Solving for EMF with $N_p = 3$ using Equation (50) gives

$$EMF_i = \frac{4}{\pi} \omega D L k_w \bar{B} N_t = \omega D L k_w B_{g1} N_t \tag{51}$$

Equation (51) can be understood as equivalent to the flux cutting form of Faraday's law:

$$E = Blv \tag{52}$$

where l is wire length and v is velocity (Ref. 14). v in Equation (52) is equivalent to the surface velocity of the machine in Equation (51) ($\frac{\omega D}{2}$). l in Equation (52) is equivalent to the machine stack length times the turn count times two ($2LN_t$) in Equation (51). k_w in Equation (51) accounts for the effectiveness of the winding at linking to the flux from the rotor to produce voltage.

3.5.2 Reactance

For surface permanent magnet machines, the *d* and *q* axis reactance's are approximately equal ($X_d \approx X_q$). Reactance should be modeled to include both the motor reactance and any AC phase filtering between the motor and its inverter. For an inductive load, reactance is given as

$$X = L * 2\pi f_{elec} \tag{53}$$

Since $X_d \approx X_q$ for a surface permanent magnet machine $L_d \approx L_q$ as long as the machine is not saturated. The inductance matrix of a machine can be written as

$$L = \begin{bmatrix} L_{aa} & L_{ab} & L_{ac} \\ L_{ab} & L_{bb} & L_{bc} \\ L_{ac} & L_{ba} & L_{cc} \end{bmatrix} \tag{54}$$

where L_{xx} are the self-inductances and L_{xy} are the mutual inductances. For a balanced and symmetric 3 phase system with no rotor salience, L can be written as

$$L = \begin{bmatrix} L_l + L_m & -\frac{L_m}{2} & -\frac{L_m}{2} \\ -\frac{L_m}{2} & L_l + L_m & -\frac{L_m}{2} \\ -\frac{L_m}{2} & -\frac{L_m}{2} & L_l + L_m \end{bmatrix} \tag{55}$$

Where L_m is the magnetizing inductance and L_l is the leakage inductance References 16 and 34. For the motor geometry discussed here L_m can be approximated using Equation (15). Using a Park transform of the induction matrix to get to the *d-q* frame, L_d, if no external filtering is used, can be written as

$$L_d = L_l + \frac{3}{2}L_m \tag{56}$$

Neglecting the leakage inductance and using Equation (23), L_d can be expanded to

$$\begin{aligned} L_d &= \frac{Slots * Layers}{2 * N_p}\frac{3}{2}N^2 * \left(\frac{2A_{tip}\mu_0}{l_{tip}} + \frac{3}{2}\frac{W_{sp}Stack\mu_0}{l_m + l_g}\right) \\ &= \frac{2 * N_p}{Layers * Slots}\frac{3}{2}N_t^2 * \left(\frac{2A_{tip}\mu_0}{l_{tip}} + \frac{3}{2}\frac{W_{sp}Stack\mu_0}{l_m + l_g}\right) \end{aligned} \tag{57}$$

where the relation between *N* and N_t is given by

$$N_t = \left(\frac{Slots * Layers * N}{2 * N_p}\right) \tag{58}$$

3.5.3 Resistance

R_s in Equations (46) and (47) is equivalent to the per phase resistance of the machine. Assuming all the machine turns are wound in series. R_s can be written as

$$R_s = \rho_{copper} * \frac{L_{Layer} * 2 * N_t}{\frac{Fill * A_{Layer} * Slots * Layers}{2 * N_t N_p}} = \rho_{copper} * \frac{L_{turn} * N_t}{A_{turn}} \tag{59}$$

where L_{turn} is the length of one turn (equal to $2L_{Layer}$) and A_{turn} is the turn area

$$A_{turn} = \frac{Fill * A_{Layer}}{N} = \frac{Fill * A_{Layer} * Slots * Layers}{2 * N_t * N_p} \tag{60}$$

3.5.4 Current

Assuming all the turns of a phase are in series, I_s can be written in terms of the current in Section 3.4 as

$$I_s = \frac{I_{peak,layer}}{N} = \frac{Slots * Layers * I_{peak,layer}}{2N_p N_t} = \frac{\pi}{2}\frac{I_{tot}}{2N_p N_t} \tag{61}$$

3.5.5 Turn Count

Substituting Equations (51), (57), (59), and (61) into Equation (49), gives

$$V_{ph} = \sqrt{\begin{aligned}&\left(\omega D L k_w B_{g1} N_t + r_{copper} * \frac{L_{Layer} * 2 * N_t}{Fill * A_{Layer}} I_{peak,layer}\right)^2 \\ &+ \left(\frac{3}{2}N_t * \left(\frac{2A_{tip}\mu_0}{l_{tip}} + \frac{3}{2}\frac{W_{sp}Stack\mu_0}{l_m + l_g}\right) I_{peak,layer}\right)^2\end{aligned}} \tag{62}$$

From Equation (62) it can be shown that $V \propto N_t$. Correspondingly the voltage of the machine can be scaled by changing turn count. Output power stays constant with changing turn count as

$$P = \frac{3}{2}EMF_i I_s = \frac{1}{2}\frac{4}{\pi}\omega D L k_w \bar{B} N_t N_p I_s = \frac{\omega D L k_w \bar{B}}{2} I_{tot} \tag{63}$$

In the absence of any effects of turn count on slot fill, efficiency also stays constant as resistive losses are independent of turn count

$$I^2R_{Loss} = N_pR_aI_{rms}^2$$
$$= N_p r_{copper} * \frac{L_{Layer} * 4 * N_p N_t^2}{Slots * Layers * Fill * A_{Layer}} \left(\frac{Slots * Layers * I_{peak,layer}}{2N_p N_t \sqrt{2}} \right)^2 \quad (64)$$
$$= Slots * Layers * r_{copper} * \frac{L_{Layer}}{Fill * A_{Layer}} I_{rms,layer}^2$$

3.5.6 Power Factor

Power Factor in the case discussed here for a surface permanent magnet synchronous machine without salience is given by

$$PF = \frac{P}{S} = \frac{\frac{3}{2} EMF_i * I_s}{\frac{3}{2} V_{ph} * I_s} = \frac{EMF_i}{V_{ph}} \quad (65)$$

3.5.7 Modulation Index

Modulation index relates motor voltage to the DC bus supply voltage. It is an important parameter for calculating current ripples and inverter switching losses when a motor is supplied by an inverter. Modulation index, m_a, is defined as

$$m_a = \frac{2V_{ph}}{V_{bus}} \quad (66)$$

4.0 Thermal Considerations

Thermal performance is the primary constraint that limits the achievable specific power of a motor. Correspondingly, any motor sizing or design that neglects thermal modeling will yield a compromised or flawed solution. For an analytical thermal model of a motor, a basic modeling approach is a thermal reluctance network model. Similar to magnetic reluctance models, this modeling approach creates thermal equivalent circuits of the motor. The fundamental equation of this modeling approach is

$$Q = \frac{\Delta T}{R} \quad (67)$$

where Q is the heat through a thermal path, ΔT is the temperature difference across the thermal path, and R is the thermal resistance of the path (Ref. 35).

4.1 Conductive Path Thermal Resistances

For conductive paths, thermal resistance, R is given by

$$R = \frac{l}{kA} \quad (68)$$

where l is the length of the path, k is the thermal conductivity of the material the path is composed of, and A is the cross sectional area of the path.

It is important to note that typically the stator iron and the stator windings are composite materials made up of metal, polymer insulations, and epoxies. Their thermal conductivities can be approximated by the rule of mixtures. For windings composed of copper, polymer insulators, and epoxy, thermal conductivity along the winding path will typically be in the range of 100 to 200 W/(mK). Thermal conductivity in the plane perpendicular to the winding path will be in the range of 0.4 to 3.0 W/(mK)

depending on slot fill and the thermal conductivity of the insulation and the epoxy. The in plane thermal conductivity of the iron will be around 20 to 50 W/(mK) while the out of plane thermal conductivity will be around 5 W/(mK).

Other important thermal resistances in the stator of the machine are the interface resistance between the winding and the iron and the iron and the housing of the machine. Between the winding and the iron of the machine there is typically a slot liner with thickness in the range of 0.05 to 0.76 mm. Aromatic polyamide paper is a common material for motor slot liners with a thermal conductivity around 0.12 W/(mK) (Ref. 36). Between the iron and the housing of the stator there is typically a bonded gap. This gap will have a thickness based on the manufacturing tolerances of the machine. A rough value of 0.1 mm can be used for initial sizing. Epoxy thermal conductivity is generally in the range of 0.2 to 1.2 W/(mK).

4.2 Fluid Flow Thermal Resistances

For convective paths, thermal resistance, *R* is given by

$$R = \frac{1}{hA} \tag{69}$$

where *h* is the convection coefficient of the flow at a liquid to solid interfaced. Values for *h* are typically found through experimentally derived Nusselt numbers.

$$Nu = \frac{hL}{k_f} \tag{70}$$

where *Nu* is the Nusselt number, *L* is the characteristic length of the flow, and k_f is the fluid thermal conductivity (Ref. 35).

For motors cooled by a propellor wake on a smooth outer mold line, the convection on the outer surface of the motor can be approximated using flat plate correlations for laminar or turbulent flow as a first approximation.

$$Nu = \begin{cases} 0.453 Re^{\frac{1}{2}} Pr^{\frac{1}{3}}, & laminar\ flow \\ 0.0308 Re^{\frac{4}{5}} Pr^{\frac{1}{3}}, & turbulant\ flow \end{cases} \tag{71}$$

where *Re* is the Reynolds number of the flow and *Pr* is the Prandtl number (Ref. 35).

For cooling flow in rectangular ducts (either finned heat sinks or cooling channels), the Nusselt number is given by

$$Nu = \begin{cases} 1.051 \ln\left(\frac{h_{fin}}{w_{channel}}\right) + 2.89, & Re_d < 3000 \\ \dfrac{\left(\frac{f}{8}\right)(Re_d - 1000)Pr}{1 + 12.7\left(\frac{f}{8}\right)^{\frac{1}{2}}\left(\mathrm{Pr}^{\frac{2}{3}} - 1\right)}, & Re_d \geq 3000 \end{cases} \tag{72}$$

where h_{fin} is the height of the duct, $w_{channel}$ is the width of the duct, and f is the Moody friction factor (Ref. 35). Moody friction factor for fully developed flow is given by

$$f = \begin{cases} \dfrac{64}{Re}, & laminar\ flow \\ (0.79 \ln(Re) - 1.64)^{-2}, & turbulant\ flow \end{cases} \tag{73}$$

Flow pressure drop can be estimated as

$$\Delta P_{flow} = \frac{(f\rho\, v^2)}{2D_h} L_{channel} \tag{74}$$

where ΔP_{flow} is the pressure drop, D_h is the hydraulic diameter, ρ is the fluid density, v is the flow velocity, and $L_{channel}$ is the length of the channel. Flow loss is given by

$$Loss_{cooling} = \Delta P_{flow} \dot{V} \tag{75}$$

Where $Loss_{cooling}$ is the power needed to pump the fluid and $\dot{V}$ is the volumetric flow rate.

Flow losses are important to track in the design of an electric motor drivetrain for aircraft applications, because

- Flow losses directly heat the fluid and correspondingly reduce the effectiveness of the cooling flow and increasing the amount of heat that needs to be rejected through a heat exchanger.
- Larger flow losses add mass to the aircraft in terms of the size of the pump needed to drive the cooling flow.
- Larger flow loss is wasted energy that reduces vehicle efficiency and requires increased energy storage to fly the same mission.

Generally laminar flow in a fine finned heat sink or direct stator cooling slots will be sufficient to cool a motor while keeping the cooling flow losses relatively small.

Convection inside the rotor cavity can have a contribution to stator cooling and is typically the primary source of rotor cooling. Estimates of rotor loss are typically neglected in initial motor sizing so it may be convenient to neglect the convective heat transfer in the internal air volume in initial motor sizing. Basic correlations for internal airgap convection are summarized here, but more complex cooling flows may be needed to maintain rotor magnet temperatures. Convection between the rotor and the stator can be broken into airgap and end space convection. For the airgap convection, the Nusselt number is given as

$$Nu = \begin{cases} 2 & , \quad Ta < 41 \\ 0.202 Ta^{0.63} Pr^{0.27} & , \quad 41 < Ta < 100 \\ 0.386 Ta^{0.5} Pr^{0.27} & , \quad 100 < Ta \end{cases} \tag{76}$$

where *Ta* is Taylor number (Ref. 37).

Convection in the end space of the motor or in the airgap of an axial flux motor can be approximated using the correlations found in Reference 38. For laminar flow *Re*<1E5

$$Nu = \begin{cases} 7.46 Re^{0.32} & , \quad G = 0.01 \\ 0.5(1 + 5.47 * 10^{-4} * e^{112G}) Re^{0.5} & , \quad G = 0.02 - 0.06 \\ 0.35 * Re^{0.5} & , \quad G > 0.06 \end{cases} \tag{77}$$

where *G* is the ratio of the axial gap to the radius of the rotor. For turbulent flow

$$Nu = \begin{cases} 0.044 Re^{0.75} & , \quad G = 0.01 \\ 0.5(12.57 e^{-33.18G}) Re^{0.6 + 25 G^{\frac{12}{7}}} & , \quad G = 0.02 - 0.06 \\ 0.0151 * Re^{0.6} & , \quad G > 0.06 \end{cases} \tag{78}$$

4.3 Example Thermal Reluctance Network

Often a 2D thermal reluctance network of a single half of one slot of the stator is sufficient for initial sizing of an electric motor. Figure 5 shows an example thermal reluctance model from Reference 11. The values used for the reluctances in terms of stator geometry and material conductivities are given in Table 2. For this level of model, some conservativism needs to be considered when sizing a motor for steady-state operation because the mesh resolution of the thermal reluctance network may not be sufficient to capture the exact hot spot of the machine and the end windings of the machine are neglected in the model.

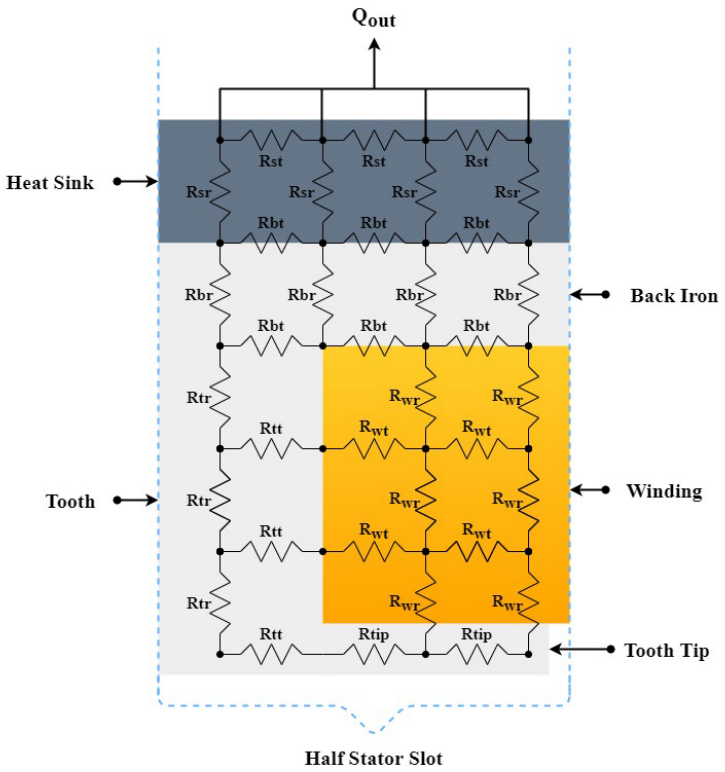

Figure 5.—Analytical Thermal Resistance Network.

TABLE 2.—THERMAL RESISTANCE DEFINITION IN ANALYTICAL THERMAL RESISTANCE NETWORK

Resistance	Definition	Resistance	Definition
$\boldsymbol{R_{wr}}$	$\frac{h_{slot}}{3} * \frac{2}{k_{w2} * W_{coil} * Stack}$	R_{br}	$\frac{t_{back}}{k_i * \frac{2\pi OR}{8Slots} * Stack}$
$\boldsymbol{R_{wt}}$	$\frac{W_{coil}}{3} * \frac{2}{k_{w2} * h_{slot} * Stack}$	R_{bt}	$\frac{2\pi OR}{8Slots} * \frac{1}{k_i * \frac{t_{back}}{2} * Stack}$
$\boldsymbol{R_{tr}}$	$\frac{h_{slot}}{3} * \frac{2}{k_i * W_{tooth} * Stack}$	R_{sr}	$\frac{t_{sink}}{k_{al} * \frac{2\pi OR}{8Slots} * Stack}$
$\boldsymbol{R_{tt}}$	$\frac{W_{tooth}}{3} * \frac{2}{k_i * h_{slot} * Stack}$	R_{st}	$\frac{2\pi OR}{8Slots} * \frac{1}{k_{al} * t_{sink} * Stack}$
$\boldsymbol{R_{tip}}$	$\frac{W_{coil}}{3} * \frac{2}{k_i * tip_t * Stack}$	----	----------

5.0 Mechanical Considerations

Major mechanical considerations in the design of a permanent magnet synchronous machine are magnet retention, windage losses, bearing sizing, rotor dynamics, and coil mechanical stress. The following sections discuss these considerations in order.

5.1 Magnet Retention

Magnet retention analysis typically needs to be the first step in the sizing of inner rotor permanent magnet electric motor since the size of the magnet retention system effects the reluctances of the magnetic circuit for the machine. For inner rotor surface permanent magnet machines, the thickness of the retaining hoop is designed to react the centrifugal forces from the magnet. The thickness of the retaining hoop is a part of the magnetic gap as shown in Figure 1. The retaining hoop's size must be accounted for in the electromagnetic sizing of the machine. Similarly for buried or interior magnet permanent magnet machines, the rotor iron is commonly used for mechanical retention of the magnets and in doing so creates leakage paths for the flux from the magnets that must be accounted for in magnetic sizing of the machines.

For the case of a surface permanent magnet retaining hoop, the peak hoop stress can be estimated as

$$\sigma = P * \frac{R_2^2 + R_1^2}{R_1^2 - R_2^2} \tag{79}$$

where P is the internal pressure created by the magnets on the hoop, R_1 is the hoop outer radius, and R_2 is the hoop inner radius. Since Equation (79) is non-linear, it can be convenient to use the thin-walled hoop stress approximation:

$$\sigma = P * \frac{R_1}{t} \tag{80}$$

where t is the radial thickness of the hoop. The pressure P in both equation forms can be estimated as

$$P = \frac{\omega^2 R_{cg} M_{mag}}{2\pi R_2 * L} \tag{81}$$

where R_{cg} is the radius of the center of gravity of a magnet in the array and M_{mag} is the total magnet mass. Often some amount of additional pressure is added when winding the hoop around the magnets so that they are compressed to the rotor and do not fracture their bond to the rotor body at high rotational speeds. At very high rotational speeds, the magnet retaining hoop may also need to preload the rotor iron so that it does not facture under its own rotationally induced stresses.

Carbon fiber hoops are common for magnet retention in aerospace motors. Design strengths for these hoops can fall in the range of 800 Mpa to 1 Gpa and enable a small magnetic airgap. Alternatively metallic hoops can be used to shield the rotor from stator current harmonics and provide better radial thermal performance from the magnets to the airgap of the machine (Ref. 39).

For sizing the rotor iron in buried or interior magnet permanent magnet machines, the calculation of stress is dependent on the geometry. For rotors with a continuous iron hoop around the magnets, the above hoop stress calculation can be used to roughly size the thickness of the iron rim around the magnets. The mass of the iron should also be included in the pressure calculation. For rotors with no outer iron rim and only an inner iron back iron. The minimum thickness of the back iron can be estimated using hoop stress calculations. Tensile stress on the iron dovetails holding the magnets in can be estimated as

$$\sigma = \frac{\omega^2 \left(M_{mag} + M_{iron}\right) R_{cg}}{t * Stack * P} k_t \tag{82}$$

where M_{iron} is the weight of the iron tabs, P is pole count, t is the minimum thickness of the tabs, and k_t is a stress concentration factor for the geometry of the thinnest section of the rotor tab. A value between 2 and 3 for k_t is likely to provide a conservative first approximation.

5.2 Windage Losses

Windage loss is the aerodynamic drag on the rotor that results from the churning of air inside the motor. Windage loss, along with magnet retention considerations, are the two primary constraints that limit the tip speed of an electric motor. Windage loss can be included as a part of speed losses in Equation (7) for a more accurate prediction of machine efficiency. For a radial airgap, the windage power loss can be approximated as

$$Loss_{wind} = kC_f \pi \rho \omega^3 r^4 Stack \tag{83}$$

where $Loss_{wind}$ is the power loss due to windage k is a roughness coefficient, C_f is the skin friction coefficient, and ρ is the air density (Ref. 32). C_f can be estimated as

$$C_f = \begin{cases} 0.515 * \dfrac{\left(\frac{ag}{R}\right)^{0.3}}{Re_{ag}^{0.5}}, & laminar\ flow \\ 0.0325 * \dfrac{\left(\frac{ag}{R}\right)^{0.3}}{Re_{ag}^{0.2}}, & turbulant\ flow\ (Re_{ag} > 10^4) \end{cases} \tag{84}$$

where ag is the size of the machine's mechanical airgap, R is the rotor radius, and Re_{ag} is the airgap Reynolds number (Ref. 40). Re_{ag} is given by

$$Re_{ag} = \frac{\omega * R * \mathrm{ag}}{\upsilon} \tag{85}$$

where ω is the angular velocity of the machine and υ is the kinematic viscosity of the air in the airgap. For the windage loss at the rotor ends $Loss_{wind}$ is defined as

$$Loss_{wind} = 0.5 C_f \rho \omega^3 (r_2^5 - r_1^5) \tag{86}$$

where $r_1$is the rotor inner radius and r_2 is the rotor outer radius. For radial motors the skin friction factors for rotors in open air can be used to approximate the windage at the rotor ends (Ref. 40).

$$C_f = \begin{cases} \dfrac{3.87}{Re_R^{0.5}}, & laminar\ flow \\ \dfrac{0.146}{Re_R^{0.2}}, & turbulant\ flow\ (Re_R > 3E5) \end{cases} \tag{87}$$

where Re_R is the tip speed Reynolds number of the machine given by

$$Re_R = \frac{\omega * R^2}{\upsilon} \tag{88}$$

5.3 Bearing Sizing

In aircraft applications, the accelerations of the aircraft and gyroscopic moments caused by the aircraft turning can lead to appreciable load on the motor bearings. Additionally, if the motor is used to direct drive a propellor, the motor bearings will be responsible for transferring the propellor loads to the rest of the aircraft structure. A free body diagram of the rotor of the motor and propellor if appropriate enables the estimation of the loads at the bearing locations. Higher accuracy can be achieved through a model that accounts for the shaft deflection. Reference 41 discusses FAA loading requirements and gives an example of aircraft load cases developed based on those requirements.

Gyroscopic moments can be a driving load for high speed aircraft motor bearing sizing. The moment can be approximated as

$$M_{gyro} = I_{gz}\omega_{motor}\omega_{aircraft} \tag{89}$$

where M_{gyro} is the gyroscopic moment, I_{gz} is the mass moment of inertia of the motor rotor assembly about its axis of rotations, ω_{motor} is the rotational speed of the motor in rad/s, and $\omega_{aircraft}$ is the pitch or yaw rate of the aircraft in rad/s.

Once loads are calculated at the bearing locations, bearing life with 90 percent reliability can be estimated as

$$L_{10} = \frac{10^6}{60 * n}\left(\frac{C}{P}\right)^k \tag{90}$$

where L_{10} is bearing life in hours, n is rotational speed in rpm, C is the dynamic load rating of the bearing, P is the equivalent dynamic bearing load, and k is a coefficient that is equal to 3 for ball bearings and 10/3 for roller bearings (Ref. 42). Equivalent dynamic load is calculated from the radial and axial load of the bearing as well as calculation factors based on the geometry of the bearing (Ref. 42). More complex equations can adjust Equation (90) to account for the lubrication condition, cleanliness, and how close the bearing is being operated to its fatigue rating (Ref. 43). L_{10} can be adjusted to L_1 (life with 99 percent reliability) by multiplying L_{10} by 1/4.

Sizing the bearings can be completed in an analytical design process by generating a database of bearings from a manufacturer catalog. Life can then be calculated for each bearing in the database and a bearing can be selected based on mass and reliability.

Often it is necessary to come up with a loading profile for the bearings and not assume their entire life is spent at peak loading conditions. In this case, total life for a bearing can be defined as

$$\frac{1}{L_{10}} = \frac{x_a}{L_a} + \frac{x_b}{L_b} + \cdots \tag{91}$$

where x_y is the percent of the bearing's life spent at a given loading condition and L_y is the lifetime the bearing has at that loading condition (Ref. 43).

When selecting bearings to minimize mass, shaft size should also be accounted for to achieve optimum results. The solved for loads in the free body diagram for the bearing can be used in Euler beam bending equations to approximate the stress in a shaft and size its thickness for a given bearing size. Stresses generated due to torque can be incorporated using linear superposition. A Von Mises yield stress calculation gives a convenient way to incorporate the multidirectional stress state into a single stress number for shaft sizing. For high speed machines, rotor dynamics, discussed in the next section, are more likely to size the shaft than mechanical stresses.

Bearing losses can be approximated using the method described in Reference 44 and incorporated as a speed loss in Equation (7). Alternatively, a simpler prediction of the friction moment can be obtained by using the equation

$$M_f = \mu R_m P \tag{92}$$

where μ is an experimentally derived bearing friction factor based on the bearing type, R_m is the mean radius in the bearing, and P is the equivalent dynamic bearing load. For ball bearings, μ will fall in the range of 0.001 to 0.0015. For roller bearings, μ can be estimated in the range of 0.0011 to 0.0018 (Ref. 45).

Bearing DN-number is defined as the bearing mean diameter times its rotational speed in RPM. It is an important number to track when sizing bearings as it relates to the feasibility of cooling the bearing with different lubrication options. Generally, grease lubrication is limited to DN-numbers less than 500,000 for lightly loaded bearings and less than 200,000 for highly loaded bearing since the grease

relubrication interval will be impractically small (Ref. 43). Oil lubrication is typically limited to less than 2 million for DN-number (Ref. 42). Bearing catalogs typically provide a reference speed and a speed limit. The reference speed is based on thermal limitations of the bearing under fairly idealized scenarios (lightly loaded) (Ref. 43). The limiting speed estimates the absolute mechanical speed limit where some portion of the bearing will fail due to centrifugal loading (Ref. 43). Designing for operation below both these bearing speeds, while a good reference for initial design, does not guarantee the bearing will perform reliably in a given application since higher loads will produce additional heat and mechanical stress in the bearings. A common pit fall in electric aircraft propulsor design are hubless rim drive motors. These are often proposed without accounting for bearing speed limits or by considering the reference/ limit speeds without understanding the idealized conditions under which those speeds were quantified.

Bearing shafts and housings must be machined to precision tolerances and provide additional stiffness to the raceways of the bearings to prevent deformation under load (Refs. 42 and 43). Not meeting these criteria can make quantification of bearing life a challenging problem. A number of known bearing failure modes result from poor fits or mounting of bearings (Ref. 46). Thermal expansion mismatch between bearing raceways and their seats and housings can lead to excess stresses or clearances in the bearing. The bearing seat tolerances generally require grinding which cannot be completed on aluminum. Correspondingly steel housings and shafts or steel sleeves/inserts will be required for bearing housings and shaft seats to enable the right tolerances, reduce thermal expansion issues, and provide adequate stiffness to the bearing raceways. Run out tolerance recommendations between different bearing seats and housings that share a common shaft is a key parameter to note when designing a motor. The recommended tolerance generally requires that all seats on a shaft or housing bearing surfaces be machined in a single setup. These considerations can drive the mechanical layout of a motor and correspondingly may improve fidelity of a motor sizing if accounted for in analytical sizing of motor drivetrains.

5.4 Rotor Dynamics

Rotor dynamics can often be the primary driver of the sizing of an electric motors shaft, bearings, and surrounding support structure. For high power machines, limits on shaft critical frequencies and bearing DN-number can limit the maximum speed a motor can be designed to operate at Reference 32.

Dunkerley (Ref. 47) developed a method for estimating shaft critical speed that can be used for a first check or sizing of the motor rotor's shaft. Special cases relevant to aircraft motors are that of a disk rotor at the center of a shaft supported at both ends and that of a shaft on its own supported at both ends. For the case of a disk rotor at the center of the shaft

$$N_c = \frac{60}{2\pi} * \sqrt{\frac{192EI}{mL^3}} \tag{93}$$

where N_c is shaft critical speed, E is the modulus of the shaft material, I is the second area moment of inertia of the shaft, m is the mass of the disk, and L is the length of the shaft between the two supports. For the shaft by itself, critical speed can be estimated as

$$N_c = 60 * 1.57 \frac{\sqrt{\frac{EI}{m}}}{L^2} \tag{94}$$

The two critical speeds can be combined to give the critical speed of the combined case as

$$\frac{1}{N_c^2} = \frac{1}{N_{c,1}^2} + \frac{1}{N_{c,2}^2} \ldots \tag{95}$$

Generally, it is a safe choice for initial motor sizing to keep the shaft first critical speed at least 2 times higher than the nominal rotational speed of the motor. It should be noted that the above assumes stiff bearings and stiff structure supporting the bearings. The critical speed is likely to drop when the stiffness of these components is accounted for in a more detailed design process. For motors not responsible for reacting propellor loads, the stiffness needed in the end bells and motor housing will likely drive their size more than stress in the components.

If there is a net radial magnetic force on a motor rotor, critical speed will be reduced since that force acts as a negative stiffness on the rotor body (force in the outward radial direction increases as deflection increases). Symmetry in the stator layout relative to the rotor can suppress this force nominally. Symmetry can be achieved through choosing slot pole combinations that have symmetry (Ref. 20). Tolerance stack-up errors will create some net radial magnetic force regardless of the symmetry in the machine. Additionally, if designing a fault tolerant machine, faulted operation will typically result in loss of symmetry in the motor and generate relatively high radial magnetic forces that will need to be accounted for in both bearing and shaft design.

5.5 Coil Thermo-Mechanical Stress

For aircraft motors, thermo-mechanical stress cycles of the motor winding insulation are potentially more limiting for the design and achievable performance of the motor than thermo-chemical aging which defines the typical insulation thermal classes. The relatively short duration and higher power associated with takeoff and climb portions of aircraft missions relative to the cruise portion limits time at maximum temperature and correspondingly can limit thermo-chemical aging of the windings while each cycle to peak temperature will generate a mechanical fatigue cycle (Refs. 11, 12, and 48). Mechanical aging and stress limits for motor winding insulation is not well defined in the open literature and is an ongoing research effort at NASA and other research institutions (Ref. 48). Regardless, a first approximation of the shear stresses generated in the motor winding insulation can be used to guide analytical machine sizing.

For the shear stress generated at the ground wall insulation the difference in coefficient of thermal expansion (CTE) and average temperature of the motor winding and the stator iron can be used to approximate the force generated at the winding to iron interface as

$$F_{shear} = A_w E_w(\alpha_w(T_w - T_0) - \alpha_i(T_i - T_0)) \tag{96}$$

where F_{shear} is the shear force at the stator iron to winding interface, A_w is the cross sectional area of the winding, E_w is the effective modulus of the winding, α_w is the effective CTE of the winding, T_w is the average temperature of the winding, T_0 is the reference temperature for the stator (the temperature the stator was cured at), α_i is the CTE of the iron, and T_i is the iron average temperature. A shear stress number can be calculated as

$$\sigma_{shear} = \frac{F_{shear}}{A_p} \tag{97}$$

where A_p is the surface area between the winding and the stator iron and σ_{shear} is a shear stress number and not an accurate prediction of stress. The above can be used as a first approximation of the stress, but higher fidelity models and/or structural FEA will be needed to obtain an accurate prediction of the stress in the stator winding. The above assumes the entire winding deflects the same amount, in actuality there will be a gradient of deflection in the winding that will result in stresses in the iron to winding interface being higher near the free ends of the contact between the two components. The stress in the turn-to-turn insulation can be approximated using a similar approach assuming the surrounding insulation and epoxy is limited in its expansion by the copper wire.

6.0 Inverter Sizing

Inverter design is one of the main constraints on the design of a high performance motor. An inverter transforms the DC power on an aircraft's electrical bus to current and voltage of the correct frequency and waveform for a given motor drive. Its ability to do so without creating excessive additional motor losses due to current ripple depends on the fundamental frequency of the electric motor, the switching frequency of the inverter, the impedance of the motor, and the impedance of the passive filters both between the inverter and the motor and between the inverted and the aircraft bus. Correspondingly, separate design of the motor and inverter for a given drive system can result in excessive added losses leading to a drive system that does not close thermally or fails to meet efficiency goals. Co-design of both will generally lead to a more optimum solution, but at a minimum design of a motor relative to the constraints of a target inverter will provide a system that closes.

The following sections discuss sizing and losses in an inverter for a given motor design. Example optimizations of inverters using similar sets of equations can be found in References 49 to 53.

6.1 MOSFET Losses

Metal-Oxide-Semiconductor Field-Effect Transistors (MOSFET) are the common switching devices used in inverters for transformation of DC bus voltage to sinusoidal currents waveforms for an electric machine via pulse width modulation (PWM). MOSFET losses are composed primarily of conduction and switching losses. Conduction losses account for the loss incurred by the switch while it is on, while switching losses account for the loss incurred during the transition between the on and off states. The methods for calculating these losses presented below can be used as a simple first approximation.

A method for calculating conduction loss based on the data sheet information of a given switching device is provided in Reference 54. Conduction loss for a single switch can be stated simply as

$$P_{cond} = \frac{1}{2} I_{RMS}^2 R_{DS,on} \tag{98}$$

where $R_{DS,on}$ is the drain-source on-state resistance and I_{RMS} is the RMS of the motor phase current. Although the motor phase current includes switching harmonics, a good approximation is to only use the fundamental frequency component. Another factor that has influence on the total conduction loss is the loss incurred by conduction through the body diode during deadtime. For increased accuracy, this can be accounted for as shown in Reference 54; however, inverters are often controlled to minimize dead time and correspondingly body diode conduction loss is typically small enough to be neglected.

The switching loss is composed as the sum of the turn-on and turn-off losses. The turn-on loss is given as

$$P_{on} = f_{sw} \frac{\left(\frac{\sqrt{2}}{\pi} I_{RMS}\right) V_{bus}}{I_{DS,test} V_{DS,test}} E_{on,test} \tag{99}$$

where f_{sw} is the inverter's switching frequency, and V_{bus} is the DC link voltage. The turn-on energy loss $E_{on,test}$, test current $I_{DS,test}$, and test voltage $V_{DS,test}$ are given in the device datasheet for a specific bus voltage and load current. The above expression uses the datasheet values to normalize the switching loss to adapt to the motor drive's operating conditions. This expression relies on the assumption that switching loss is linearly dependent on the bus voltage and load current. If increased accuracy is needed, the switching loss figures given in the device datasheet can be curve-fit to better represent nonlinear behavior not captured in these equations.

Similarly, the turn-off loss can be expressed as

$$P_{off} = f_{sw} \frac{\left(\frac{\sqrt{2}}{\pi} I_{RMS}\right) V_{bus}}{I_{DS,test} V_{DS,test}} E_{off,test} \tag{100}$$

where $E_{off,test}$ is the turn-off energy loss at the specified test conditions.

Finally, the reverse recovery loss of the body diode can also be taken into consideration. From Reference 55, the reverse recovery loss can be expressed as

$$P_{rr} = \frac{1}{4} Q_{rr} V_{bus} f_{sw} \tag{101}$$

where Q_{rr} is the reverse recovery charge which can be obtained from the device datasheet.

The sum of all losses for a single switching device is the total of all the conduction and switching losses

$$P_{loss,sw} = P_{cond} + P_{on} + P_{off} + P_{rr} \tag{102}$$

and the total loss for a conventional six switch motor drive (2 switches per phase on a three phase motor) is simply $6P_{loss,sw}$.

6.2 Ripple Current

For a purely inductive load, ripple current at the output of the inverter can be estimated as

$$I_{ripple} = \frac{V_{bus}}{2} * \frac{m_a}{2\sqrt{3}L} * \frac{1}{f_{sw}} \tag{103}$$

where m_a is modulation index, L is the phase inductance, and f_{sw} is the switching frequency (Ref. 56). A target I_{ripple} can be used to define the size of the filters at the outputs of the inverter. Magnetic reluctance circuit analysis can be used to define the inductors size and loss. Typically, some number of distributed small airgaps or a tuned ferrite core material is used for these inductors to reduce the permeability of the core and enable the design of the core to be practical without exceeding current density limits in the winding around the core. Nawawi et al. (Ref. 53) give equations defining the minimum winding area within a core needed for a given inductance, core max field, max per turn current, winding fill percentage, and core cross sectional area.

$$W_a \geq (2 * L * \frac{I_0 A_w}{(B_{max} * Fill * A_c)}) \tag{104}$$

where, W_a is winding area, I_0 is the phase peak current in the inductor, A_w is the area of the wire, B_{max} is the maximum flux density allowed in the core material, $Fill$ is the winding fill factor, and A_c is the core cross sectional area. The number of turns can then be calculated as

$$N = \frac{I_0 L}{B_{max} A_c} = \frac{I_0 L}{\varphi} \tag{105}$$

The relationship between required inductance, inductor effective permeability, and inductor flux path length is given by

$$L = \frac{A_c \mu N}{l_{path}} \tag{106}$$

where μ is the effective permeability of the inductor accounting for airgaps and l_{path} is the length of the flux path in the iron. l_{path} relates to W_a through the geometry of the inductor. For a toroidal path, l_{path} solves to

$$l_{path} = 2\pi^{\frac{1}{2}} W_a^{\frac{1}{2}} \tag{107}$$

The above relation between L and μ assumes that all the flux is contained within the core. Leakage flux will contribute some additional inductance to the inductor depending on the geometry of the winding (Ref. 57). If the value of μ is not significantly larger than that of air or large airgaps are used to reduce μ to a target value, flux leakage will be significant and a more complex magnetic reluctance network may be needed to compute inductance.

The length of the wire used to form a turn in the inductor relates to A_c through the assumed geometry of the inductor. The minimum length being given by the perimeter of the assumed core cross section. The resistive loss per inductor in the winding can be estimated as

$$Loss_{I^2R} = N * r_{copper} \frac{l_w}{A_w} \frac{I_0^2}{2} \tag{108}$$

where l_w is the length of each turn around the inductor. AC winding losses will contribute some additional loss to the inductor winding especially if large amounts of leakage flux are present. They are neglected here as the use of litz wire and good inductor design can minimize them to relatively small values. The possibility of additional AC losses should be noted when completing inductor sizing with the above method.

Iron losses in the inductor will result from both the ripple current and the fundamental component of the current. Equation (27) or (28) for iron loss above can be used to approximate the iron loss in the inductors; however, the likely large difference in the switching frequency and the fundamental frequency may require two separate curve fits to supplier provided iron loss data. In general, it is likely that the switching frequency will be sufficiently high such that the skin depth of the eddy currents in the iron is less than the size of the iron laminations. Corrections for skin effect like those presented in Reference 26 may be used to adjust iron loss equations to account for skin effect.

The above inductor sizing equations are for a purely inductive AC filter on the output of the inverter. LCL filters are also a common choice for AC filters at the output of voltage source inverters (Refs. 50, 53, and 51). Nawawi (Ref. 53) provides a sizing methodology for filters of this type.

Current ripple will couple into the motor and cause additional AC resistive, iron, and magnet losses. For initial sizing, neglecting those losses is reasonable; however, a more detailed analysis is typically needed for a final motor design. To fully capture the effect of stator current ripple harmonics on the losses in the motor, a transient FEA model is likely required as the ripple frequency may result in a skin depth well below the size of the magnetic components in the motor. A first approximation of the current ripple effect on the field in the magnets and the stator iron can be made using the model for stator inductance in Section 3.2.1.2. Reference 58 provides an example of analytical co-design of a motor and inverter accounting for ripple current effects on motor losses.

6.3 DC Link Capacitor

The current in the DC link capacitor can be estimated as

$$I_{c,rms} = \sqrt{I_{In,rms}^2 - I_{In,avg}^2} \tag{109}$$

where $I_{c,rms}$ is the root meant squared capacitor current, $I_{In,rms}$ is the root mean squared inverter input current, and $I_{In,avg}$ is the average inverter current (Ref. 59). $I_{In,rms}$ can be estimated as

$$I_{In,rms} = I_{ph,rms} \sqrt{\frac{2\sqrt{3}}{\pi} m_a (PF^2 + \frac{1}{4})} \tag{110}$$

where $I_{ph,rms}$ is the motor phase root mean squared current and *PF* is the power factor of the motor circuit accounting for external passive filters. $I_{In,avg}$ is given as

$$I_{In,avg} = \frac{3}{4} I_0 * m_a * PF \tag{111}$$

The needed capacitance to limit voltage ripple on the supply side to a desired value can be defined as

$$C = \frac{I_{c,rms}}{dV * f_{sw}} \tag{112}$$

where dV is the target max voltage ripple on the capacitor. In general, the desired maximum voltage ripple limit on the capacitor is system design dependent. Capacitor voltage ripple will cause additional electrical stresses on other components that share a bus with the motor drive. Additionally, the resulting current ripple on the bus caused by the ripple at the capacitor can generate electromagnetic interference throughout the aircraft's electrical systems. Bus/supply filters will work with the capacitors to limit the current ripple on the bus but may not be sized/designed at the start of initial motor drivetrain design. If no system level requirement or supply design is defined for initial sizing, 1 percent voltage ripple may be a good starting point.

Losses in the capacitor due to the current ripple it experiences can be estimated as

$$Loss_{cap} = R_{cap} I_{c,rms}^2 \tag{113}$$

where R_{cap} is the equivalent series resistance of the capacitor.

A method for estimating capacitor size, mass, and equivalent series resistance is to build a database of off the shelf capacitors with the required voltage rating and stack them in series and parallel (Refs. 50 and 51). R_{cap} depends on frequency as is shown in the data in Reference 60. Lockett and He (Ref. 50), provide a method for estimating R_{cap} at a given frequency based on data sheet available capacitor dissipation factors as

$$R_{cap,f} = \frac{\tan(\delta)}{2\pi f * C} \tag{114}$$

where $R_{cap,f}$ is the capacitor's equivalent series resistance at frequency f and $\tan(\delta)$ is the dissipation factor of the capacitor. With the single assumed current value above, $I_{c,rms}$, f should be assumed to be the switching frequency. A more complete estimation of all DC-link capacitor current harmonics can be computed by following the method in Reference 61. As is shown in Reference 50, accounting for all harmonics changes Equation (114) into a sum over all frequencies.

6.4 Thermal Modeling

Inverter component thermal limits constrain the maximum specific power of an inverter and in some instances heat sink mass can be a dominant source of mass in an inverter design. Inverter switches in particular represent small, localized heat sources with thermal limits in the 120 °C range for silicon carbide. If cooled by a heat sink, the thermal resistance internal to the switch (junction to case resistance) and the contact resistance between the switches and their heat sink (case to sink resistance) can be the dominant thermal resistances. Simple one-dimensional thermal network models are commonly used to size heatsinks for inverter switches (Refs. 49, 50, 51, and 53). Figure 6 shows a common layout of this one-dimensional model.

T_s in Figure 6 is the switch temperature while *Ta* is the coolant temperature. Inverter data sheets will define junction to case thermal resistance R_{j-c} and provide switch dimensions that can be used to design the thermal interface between the switch and the sink and its thermal resistance R_{c-s}. Sink to coolant thermal resistance can be defined by sizing a heatsink design using the equations in Section 4.2. Due to

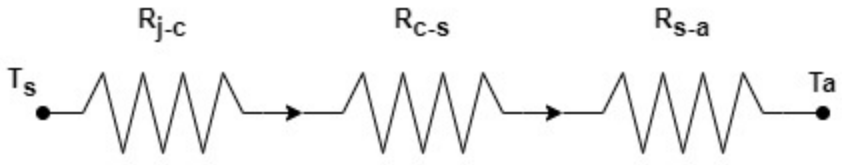

Figure 6.—Common One-Dimensional Thermal Network Model for Inverter Switch Temperature.

the small size of switching devices, care must be taken to appropriately account for conduction through the heat sink when calculating the heated area of the sink. Commonly heat pipes are used as heat spreaders in inverter heatsinks to improve the heated area of the sink by the switch.

Both absolute temperature and thermal cycling contribute to the failure of inverter switching devices. Differential thermal expansion of components within a switching device can cause mechanical failure of joints within the switching device (Refs. 50 and 62). An estimate of device lifetime as a function of junction average temperature, temperature change during a power cycle, and switch on time can be found in Reference 62. The model depends on a number of device specific constants that may not be available at the sizing stage of an inverter since determining the constants requires specific lifetime testing a given device.

DC link capacitors also are a known cause of thermal failure of inverters. Typically, capacitors will have a defined case limit temperature in their data sheet. This temperature along with a thermal contact model and heat sink design can be used in a one-dimensional thermal model of the capacitors. Reference 50 provides an equation for estimating capacitor lifetime as a function of operating temperature and the applied electrical stress. Even with good thermal design, as is noted in Reference 50, it may be necessary to stack multiple redundant capacitors in parallel to achieve sufficient reliability in an aircraft motor drive.

Inverter inductor thermal performance can be modeled using a one or two-dimensional thermal reluctance networks. Similar to the motor thermal modeling, the inductor's windings thermal conductivity can be approximated using rule of mixtures. The inductor iron's thermal property can also be approximated with rule of mixtures. The assumed geometry of the inductor will determine how the inductor thermal model should be developed. Similar to what was done for the motor, thermal contacts between the inductor and the heat sink should be accounted for as well as the ground wall insulation between the core and the winding. Generally, since inductors will have much greater max use temperatures, similar to the temperature limits of the motor winding, it is unlikely that the inductor will have thermal design issues if designed to share a heat sink with the switches and the capacitors of the inverter.

7.0 Conclusions

This paper presents models and discusses aspects for consideration relative to the preliminary sizing and design of electric motors and inverters in the context of application to aircraft propulsion systems. The paper is intended as an aid for developing an understanding of basic electric motor sizing and design principles. Ongoing research and the corresponding follow on publications by the authors will cover design tool examples, different electric motor topologies, and more advanced motor/inverter technologies.

References

1. K.P. Duffy and R.H. Jansen, “Turboelectricand Hybrid Electric Aircraft Drive Key Performance Parameters,” in *AIAA/IEEE Electric Aircraft Technologies Symposium (EATS)*, Cincinnati, 2018.
2. R.H. Jansen, G.V. Brown, J.L. Felder, and K.P. Duffy, “Turboelectric Aircraft Drive Key Performance Parameters and Functional Requirements,” NASA/TM—2016-218919, Cleveland, 2016.
3. W. Johnson, C. Silva, and E. Solis, “Concept Vehicles for VTOL Air Taxi Operations,” in *American Helicopter Society Technical Conferance on Aeromechanics Design for Transfromative Vertical Flight*, San Francisco, 2018.
4. C. Silva, W. Johnson, K. Antcliff, and P.D. Michael, “VTOL Urban Air Mobility Concept Vehicles for Technology Development,” in *AIAA Aviation*, Alanta, 2018.
5. E. Hendricks, E. Aretskin-Hariton, D. Ingraham, J. Gray, S. Schnulo, J. Chin, R. Falck, and D. Hall, “Multidisciplinary Optimization of an Electric Quadrotor Urban Air Mobility Aircraft,” in *AIAA Aviation*, 2020.
6. A.D. Anderson, N.J. Renner, Y. Wang, D. Lee, S. Agrawal, S. Sirimanna, K. Haran, A. Banerjee, M. Starr, and J. Felder, “System Weight Comparison of Electric Machine Topologies for Electric Aircraft Propulsion,” in *AIAA/IEEE Electric Aircraft Technologies Symposium*, Cincinnati, 2018.
7. Z. Cheng, S. Zhao, L. Scotzniovsky, G. Rodriguez, C. Mi, and J. Hwang, “A Differentiable Method for Low-Fidelity Analysis of Permanent-Magnet Synchronous Motors,” in *AIAA SciTech Forum*, National Harbor, MD, 2023.
8. A. Dannier, E. Fedele, and M. Coppola, “Sizing approach of high torque density motors for aircraft application,” in *International Symposium on Power Electronics, Electrical Drives, Automation and Motion*, Sorrento, Italy, 2020.
9. J. Swanke, D. Bodda, T. Jahns, and B. Sarlioglu, “Comparison of Modular PM Propulsion Machines for High Power Density,” *IEEE Transportation Electrification Conference and Expo (ITEC)*, pp. 1–7, 2019.
10. M. Boyd, K. Yost, and S. Patnaik, “Tradespace Exploration of Electrified Propulsion and More-Electric Aircraft Generators,” in *AIAA Propulsion and Energy Forum*, VIRTUAL EVENT, 2020.
11. T.F. Tallerico, “NASA Reference Motor Designs for Electric Vertical Takeoff and Landing Vehicles,” in *AIAA Propulsion and Energy 2021 Forum*, Virtual, 2021.
12. T.F. Tallerico, J. Chapman, and A.D. Smith, “Preliminary Electric Motor Drivetrain Optimization Studies for Urban Air Mobility Vehicles,” in *AIAA/IEEE Electric Aircraft Technologies Symposium*, Anaheim, 2022.
13. T.F. Tallerico, A.D. Smith, J.T. Thompson, E.L. Pierson, C.A. Hilliker, D. Avanesian, W. Miller, and K.W. Monaghan, “Outer Mold Line Cooled Electric Motors for Electric Aircraft,” in *AIAA/IEEE Electric Aircraft Technologies Symposium*, Virtual, 2020.
14. A. Hughes and B. Drury, Electric Motors and Drives, Waltham, MA: Elsevier Ltd, 2013.
15. T.A. Lipo, INTRODUCTION TO AC MACHINE DESIGN, Piscataway, NJ: IEEE Press, 2017.
16. P. Krause, O. Wasynczuk, S. Sudhoff, and S. Pekarek, Analysis of Electric Machinery and Drive Sytems, Hoboken: John Wiley & Sons, Inc., 2013.
17. G.V. Brown, A.F. Kascak, B. Ebihara, D. Johnson, B. Choi, M. Siebert, and C. Buccieri, “NASA Glenn Research Center Program in High Power Density Motors for Aeropropulsion,” NASA, Cleveland, 2005.
18. T.F. Tallerico, “Genetic Optimization of Planetary Gearboxes Based on Analytical Gearing Equations,” NASA, Cleveland, 2022.
19. J.J. Coy, D.P. Townsend, and E.V. Zaretsky, “Gearing,” NASA, Cleveland, 1985.

20. F. Libert and J. Soulard, “Investigation on Pole-Slot Combinations for Permanent-Magnet Machines with Concentrated Windings,” Royal Institute of Technology, 2004.
21. Z.P. Xia, Z.Q. Zhu, and D. Howe, “Analytical Magnetic Field Analysis of Halbach Magnetized Permanent-Magnet Machines,” *IEEE TRANSACTIONS ON MAGNETICS*, vol. 40, no. 4, 2004.
22. Arnold Magnetic Technologies, “Temperature Effects on Magnetic Output,” 2015. [Online]. Available: https://www.arnoldmagnetics.com/wp-content/uploads/2017/10/TN_0303_rev_150715.pdf. [Accessed 30 5 2023].
23. C.P. Steinmetz, “On the Law of Hysteresis,” *Transactions of the American Institute of Electrical Engineers*, vol. 9, no. 1, pp. 1–64, 1892.
24. ASTM, “A697/A697M: Standard Test Method for Alternating Current Magnetic Properties of Laminated Core Specimen UIsing Voltmete-Ammeter-Wattmeter Methods,” 2018.
25. G. Bertotti, F. Fiorillo, and G.P. Soardo, “THE PREDICTION OF POWER LOSSES IN SOFT MAGNETIC MATERIALS,” *JOURNAL DE PHYSIQUE*, vol. 49, no. C-8, pp. 1915–1919, 1988.
26. A. Boglietti, A. Cavagnino, M. Lazzari, and M. Pastorelli, “Predicting Iron Losses in Soft Magnetic Materials With Arbitrary Voltage Supply: An Engineering Approach,” *IEEE TRANSACTIONS ON MAGNETICS*, vol. 39, no. 2, pp. 981–989, 2003.
27. A. Krings and J. Soulard, “Overview and Comparison of Iron Loss Models for Electric Machines,” *Journal of Electrical Engineering*, vol. 10, pp. 162–169, 2010.
28. J.A. Ferreira, “Improved Analytical Modeling of Conductive Losses in Magnetic Components,” *IEEE TRANSACTIONS ON POWER ELECTRONICS*, vol. 9, no. 1, pp. 127–131, 1994.
29. N.J. Salk and C.M. Cooke, “Calculation of AC Losses in Multi-phase Litz Coil Systems,” in *IEEE Transportation Electrification Conference & Expo (ITEC)*, Anaheim, CA, 2022.
30. C.R. Sullivan and R.Y. Zhang, “Simplified Design Method for Litz Wire,” *IEEE Applied Power Electronics Conference (APEC)*, pp. 2667–2674, 2014.
31. T. Zou and et al., “A Comprehensive Design Guideline of Hairpin Windings for High Power Density Electric Vehicle Traction Motors,” *IEEE Transactions on Transportation Electrification*, vol. 8, no. 3, pp. 3578–3593, 2022.
32. A. Borisavljevic, “High-Speed PM Machines: Applications, Trends, and Limits,” in *Limits, Modeling, and Design of High-Speed Permanent Magnet Machines*, Berlin, Springer, 2013, pp. 13–27.
33. M.A. Masoum and E.F. Fuchs, Power Quality in Power Systems and Electric Machines, London: Elseveir Inc., 2015.
34. M. C. T. a. W. S. Y. S. T. Wu, “Investigation of Correlations of Direct-Quadrature Axis Inductance with Magnetizing Inductance and Inductance Variation for Permanent-Magnet Synchronous Motor,” in *21st International Conference on Electrical Machines and Systems (ICEMS)*, Jeju, Korea (South), 2018.
35. T.L. Bergman, A.S. Lavine, F.P. Incropera, and D.P. Dewitt, Introduction to Heat Transfer, Hoboken: John Wiley & Sons, 2011.
36. Dupont, “DuPont Nomex 410 Technical Data Sheet,” 2016. [Online]. Available: https://www.dupont.com/content/dam/dupont/amer/us/en/safety/public/documents/en/DPT16_21668_Nomex_410_Tech_Data_Sheet_me03_REFERENCE.pdf. [Accessed 5 June 2023].
37. D.A. Staton and A. Cavagnino, “Convection Heat Transfer and Flow Calculations Suitable for Analytical Modelling of Electric Machines,” in *32nd Annual Conference on IEEE Industrial Electronics*, Paris, 2006.
38. D.A. Howey, P.R.N. Childes, and A.S. Holmes, “Air-Gap Convection in Rotating Electrical Machines,” *IEEE Transactions on Industrial Electronics*, vol. 59, no. 3, 2012.

39. M.K. Islam, K.N. Taasnim, S. Choi, S. Kwak, and A. Arafat, “Designing High-Power Ultra-High-Speed Motor Using a New Multiphysics Multi-Objective Optimization Method for Mechanical Antenna Applications,” *IEEE Access*, vol. 10, pp. 106305–106323, 2022.
40. J. Saarie, “Thermal Analysis of High-Speed Induction Machines,” in *Ph.D. Dissertation, Acta Polytechnica Scandinavica*, 1998.
41. L. Miller, R. Jansen, and A. Dimston, “Structural Requirements for Design and Analysis of 25% Scale Subsonic Single Aft Engine (SUSAN) Research Aircraft,” in *AIAA SciTech Forum*, National Harbor, 2023.
42. SKF Group, “SKF Super Precision Bearing Catalog,” March 2016. [Online]. Available: https://www.skf.com/binaries/pub12/Images/0901d19680495562-Super-precision-bearings-catalogue---13383_2-EN_tcm_12-129877.pdf. [Accessed July 2020].
43. SKF Group, “SKF Rolling Bearing Catalog,” October 2018. [Online]. Available: https://www.skf.com/binary/77-121486/SKF-rolling-bearings-catalogue.pdf. [Accessed January 2020].
44. SKF Group, “SKF model for calculating the frictional moment,” [Online]. Available: https://www.skf.com/binary/12-299767/0901d1968065e9e7-The-SKF-model-for-calculating-the-frictional-movement_tcm_12-299767.pdf. [Accessed January 2020].
45. J. Shigley and C. Mischke, “Rolling Contact bearings,” in *Standard Handbook of Machine Design*, New York, McFraw-Hill Inc., 1986, pp. 27.1–27.17.
46. SKF Group, “Bearing Damage and Failure Analysis,” June 2017. [Online]. Available: https://www.skf.com/binaries/pub12/Images/0901d1968064c148-Bearing-failures---14219_2-EN_tcm_12-297619.pdf. [Accessed April 2023].
47. S. Dunkerley, “On the whirling and vibration of shafts,” *Philosophical Transactions of the Royal Society of London*, vol. 185, pp. 279–360, 1894.
48. T. Tallerico, T. Krantz, M. Valco, and J. Salem, “Urban Air Mobility Electric Motor Winding Insulation Reliability: Challenges in the Design and Qualification of High Reliability Electric Motors and NASA’s Research Plan,” NASA, Cleveland, 2022.
49. M. Hassan, Z. Yuan, H. Peng, A.I. Emon, Y. Chen and F. Luo, “Model Based Optimization of Propulsion Inverter for More-Electric Aircraft Applications Using Double Fourier Integral Analysis,” in *2020 AIAA/IEEE Electric Aircraft Technologies Symposium (EATS)*, New Orleans, LA, 2020.
50. B. Luckett and J. He, “Reliability-Oriented Multi-Objective Design Optimization of Electric Aircraft Propulsion Drives,” in *IEEE Energy Conversion Congress and Exposition (ECCE)*, Detroit, MI, USA, 2022.
51. R. Lai and et. al., “A Systematic Topology Evaluation Methodology for High-Density Three-Phase PWM AC-AC Converters,” *IEEE Transactions on Power Electronics*, vol. 23, no. 6, pp. 2665–2680, 2008.
52. M. Hassan, Z. Yuan, A. Emon, and F. Luo, “A Framework for High Density Converter Electrical-Thermal-Mechanical Co-design and Co-optimization for MEA Applications,” in *IEEE Energy Conversion Congress and Exposition (ECCE)*, 2021.
53. A. Nawawi and et. al., “Design and Demonstration of High Power Density Inverter for Aircraft Applications,” *IEEE Transactions on Industry Applications*, vol. 53, no. 2, pp. 1168–1176, 2017.
54. E. Gurpinar and B. Ozpineci, “Loss Analysis and Mapping of a SiC MOSFET Based Segmented Two-Level Three-Phase Inverter for EV Traction Systems,” in *2018 IEEE Transportation Electrification Conference and Expo (ITEC)*, Long Beach, CA, 2018.

55. D. Graovac, M. Purschel, and K. Andreas, “MOSFET Power Losses Calculation Using the Data-Sheet Parameters,” July 2006. [Online]. Available: https://www.digchip.com/application-notes/48/41484.php. [Accessed December 2021].
56. G. Grandi and J. Loncarrski, “Evaluation of Current Ripple Amplitude in Three-Phase PWM Voltage Source Inverters,” in *International Conference-Workshop Compatibility And Power Electronics*, 2013.
57. M.J. Nave, “On modeling the common mode inductor,” in *International Symposium on Electromagnetic Compatibility*, NJ, 1991.
58. X. Zhang and K. Haran, “Optimization Methodology for High Frequency, Slotless PM Synchronous Machines Based on Drive System Co-Design,” in *IEEE International Electric Machines and Drives Conference (IEMDC)*, San Francisco, 2023.
59. J.W. Kolar, T.M. Wolbank, and M. Schrodl, “Analytical calculation of the RMS current stress on the DC link capacitor of voltage DC link PWM converter systems,” in *Ninth International Conference on Electrical Machines and Drives*, 1999.
60. Vishay Roederstein, “Metallized Polypropylene Film Capacitor AC Filtering Radial Type,” 19 May 2021. [Online]. Available: https://www.vishay.com/docs/28172/mkp1847ac.pdf. [Accessed 25 April 2023].
61. B.P. McGrath and D.G. Holmes, “A General Analytical Method for Calculating Inverter DC-Link Current Harmonics,” *IEEE Transactions on Industry Applications*, vol. 45, no. 5, pp. 1851–1859, 2009.
62. Semikron, “Application Note AN 21-001: Power Cycle Model for IGBT Product Lines,” 24 8 2021. [Online]. Available: https://www.semikron-danfoss.com/service-support/downloads/detail/semikron-application-note-power-cycle-model-for-igbt-product-lines-en-2021-08-24-rev-01.html. [Accessed 26 4 2023].